On the correlation of temperature harmonic content with energy dissipation in C45 steel samples under fatigue loading

Riccardo Cappello[a], Giovanni Meneghetti[b], Mauro Ricotta[b], Giuseppe Pitarresi[a,*]

[a]*Department of Engineering (DING), University of Palermo, Viale delle Scienze, 90128 Palermo, Italy*
[b]*Department of Industrial Engineering, University of Padova, via Venezia, 1, 35131 Padova, Italy*

Abstract

Fatigue damage onset involves a transformation of mechanical energy. This is in part spent into work of plastic deformation and fracture and in part transformed into heat. Therefore, different thermomechanical heat sources are activated during a fatigue loading cycle, resulting in a temperature modulation that can be characterized by its frequency content. Several studies have monitored the temperature on samples undergoing high-cycle fatigue, measuring specific thermomechanical metrics which could serve as indicators of damage evolution. The present work evaluates the harmonic content of temperature, to investigate its correlation with the material dissipation. The harmonic terms investigated are the amplitude and phase of temperature at the loading frequency (First Harmonic) and at twice the loading frequency (Second Harmonic). The paper reviews the mechanisms linking the evolution of heat dissipation to changes in these four parameters. The theoretical analysis is supported by an experimental campaign carried out on C45 steel tensile specimen subject to $R = -1$ and $R = 0.1$ loading ratios. The harmonic metrics are evaluated analyzing both their spatially averaged value and their spatial dispersion, to check for the formation of localized heat dissipation zones in early fatigue life. The study shows that the

*Corresponding author
Email address: giuseppe.pitarresi@unipa.it (Giuseppe Pitarresi)

phase of the Second Harmonic signal has a peculiar bimodal distribution that can be correlated to either a thermoelastic or dissipative prevailing effect. This behavior evolves towards a unimodal dissipative behavior when the load amplitude is increased, thus proposing the Second Harmonic phase parameter as an effective indicator for monitoring internal intrinsic dissipation in the material.
Keywords: Thermomechanics, Fatigue, Dissipative heat sources, Thermoelastic Effect, Frequency Domain Analysis

---

Highlights

- Heat dissipation at early fatigue stages is correlated to temperature harmonics.
- Mechanisms correlating the First Harmonic to heat dissipation are highlighted.
- Thermoelastic and dissipative heat sources induce different Second Harmonic phases.
- The phase of the Second Harmonic has a bimodal distribution.
- Early fatigue-induced intrinsic heat dissipation is a non-localized phenomenon.

List of Symbols

A_x	Thermodynamic force associated to the internal variable x
C_p, C_ε	Specific heats at constant pressure, volume $[\frac{\mathrm{J}}{\mathrm{kg}\cdot\mathrm{K}}]$
d	Subscript used to indicate a dissipation related quantity
D	Amplitude of the second harmonic of temperature [K]
D_m	Intrinsic mechanical dissipation $[\frac{\mathrm{W}}{\mathrm{m}^3}]$
E	Young's modulus [MPa], or alternatively the amplitude of the first harmonic or temperature [K]

E_{2L}	Amplitude of thermoelastic signal induced by the load harmonic at angular frequencies 2ω [K]
FH	Harmonic of temperature at the angular frequencies ω
f_L	Loading Frequency [Hz]
H	Helmholtz potential $[\frac{\mathrm{J}}{\mathrm{kg}}]$
K_o, K_1, K_2	Thermoelastic constants in the first and second order theories $[\frac{1}{\mathrm{MPa}}]$, $[\frac{1}{\mathrm{MPa}^2}]$, $[\frac{1}{\mathrm{MPa}^2}]$
$L_\omega, L_{2\omega}$	Amplitude of the load signal harmonics at the angular frequencies ω and 2ω
R	Amplitude of the harmonic of temperature at the angular frequencies 3ω [K]
SH	Harmonic of temperature at the angular frequencies 2ω
T	Absolute body temperature [K]
T_o	Mean body temperature [K]
$\mathbf{x}$	Vector of internal system variables
5^{th}	Index for the 5^{th} percentile of a distribution
95^{th}	Index for the 95^{th} percentile of a distribution
α	Coefficient of thermal expansion , $[\frac{1}{\mathrm{K}}]$
γ	Lame's elastic constant , $[\frac{\mathrm{MPa}}{\mathrm{K}}]$
δ_{ij}	Kronecker delta operator
ΔT_{th}	Thermoelastic signal amplitude [K]
ρ	Material density , $[\frac{\mathrm{kg}}{\mathrm{m}^3}]$
σ_a	specimen stress amplitude under uniaxial sinusoidal loading
σ_m	specimen mean stress under uniaxial sinusoidal loading [MPa]
Φ_D	Phase of the Second Harmonic SH [°]
Φ_L	Phase of the load harmonic at the angular frequencies ω [°]
Φ_E	Phase of the First Harmonic FH [°]
ω	Angular frequency of the load fundamental harmonic $[\frac{\mathrm{rad}}{\mathrm{s}}]$

1. Introduction

Knowledge of the mechanisms leading to fatigue failure is a fundamental design need accompanying the development of a new material or fabrication process. Traditional experimental characterization schemes to investigate the fatigue behavior require significant time and resources [1, 2] and may act as a bottleneck in the continuous quest for better performing structural materials. A significant research effort is therefore devoted to improving methodologies to assess the fatigue behavior in a faster and less expensive manner.

Since the last 20 years, methods based on Infrared Thermography have been proposed to perform rapid non-contact full-field monitoring of temperature evolution during fatigue cycling of materials and components [3–5]. It is observed that damage onset requires a transformation of the inputted strain energy, which in part is spent to produce irreversible structural changes and in part is transformed into heat [6]. The temperature changes arising from this heat can be effectively monitored on the surface of the sample by means of infrared cameras.

Some authors have explored the possibility to correlate the material fatigue damage evolution and the fatigue limit with thermomechanical metrics, see e.g. [2–23] and Figure 1 for a schematic representation of the measuring approach. As the material energy dissipation increases with the applied load amplitude, these thermomechanical metrics start to grow at a higher rate, allowing to detect heat dissipation at an early stage of the fatigue life [4, 5]. A common attempt carried out in many studies has been that of proposing a rapid Fatigue Limit estimations through Thermographic Methods (here abbreviated as FLTM)[10]. The surface temperature of a cycling coupon is sampled by IR cameras, and time derivatives of the initial temperature increase, or the average temperature of plateaus settling at thermal equilibrium are typical thermal parameters that have been proposed to uncover early material irreversible transformations. In this scheme, the load amplitude is progressively increased in a stepwise manner, and the temperature is monitored within each loading block. Figure 1a provides a scheme of a typical FLTM measuring approach. Different thermomechanical

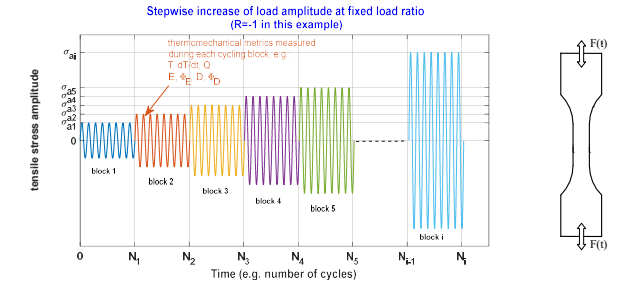

(a)

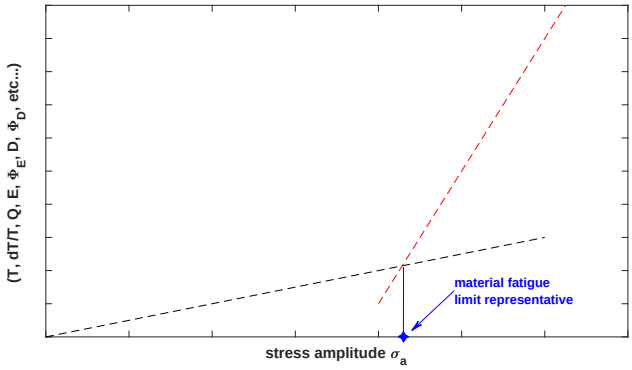

(b)

Figure 1: schematic representation of the measuring approach of thermographic methods for the estimation of fatigue limits. (a) stepwise sequence in fatigue cycling; (b) evaluation of the trends of thermomechanical metrics.

metrics can be derived from the measured temperature within each loading block, and successively analyzed as shown in Figure 1b, where anomalous rate changes are sought and correlated to the fatigue damage evolution and the material fatigue limit [2–7, 9–20, 22–28].

It is observed that metrics based on the absolute temperature may be affected by environmental conditions or measurement inaccuracies, which can impair the repeatability and reproducibility of the experimental technique [18, 23]. In fact, the absolute temperature can be influenced by ambient conditions and heat conduction through the testing machine grips. Moreover, infrared cameras show a rather poor accuracy when measuring absolute temperatures, in part due to

inherent inaccuracies in modelling the material emissivity behavior. They, instead, may achieve remarkable sensitivities when it comes to detect temperature changes. This is the case with cooled IR sensors, which exhibit low Net Equivalent Temperature Difference (NETD). Moreover, the high frame rate of cooled sensors enables the possibility to effectively sample temperature over time, thus enabling a time averaging filtering which further improves the NETD sensitivity. This is, for instance, exploited in Thermoelastic Stress Analysis (TSA), where temperature changes below 1 mK can be detected [29, 30]. It is therefore useful to propose temperature metrics related with temperature changes at specific loading frequencies. A number of works, including the present one, have then propsed to investigate the influence of the heat sources on the temperature modulation by means of frequency domain signal processing strategies [2, 6, 7, 9, 10, 16, 18, 20–26, 31–33].

The correlation between the spatial-temporal temperature evolution and the thermomechanical energy coupling sources is well described by the heat diffusion equation derived from the theory of thermodynamics of irreversible processes for solid materials [6, 15, 34, 35]. According to this, when a metallic material is cyclically loaded within the elastic field under adiabatic conditions, the only heat source involved is the thermoelastic effect, which gives rise to a temperature modulation at the same loading frequency. This is hereinafter called First or Fundamental Harmonic (FH). As soon as heat dissipation and irreversible damages are initiated, other irreversible heat source terms come into play. When this happens, the thermoelastic law gradually ceases to fully model the temperature changes, and other harmonics arise due to the heat dissipation evolution within each loading cycle. Enke [36], in particular, suggested that the irreversible heat produced by dissipation reaches a maximum nearby each peak and trough of the loading wave, therefore introducing a modulation in the temperature fluctuation which has a significant peak at twice the loading frequency, hereinafter called Second Harmonic (SH). A theoretical justification of the modulation of temperature into higher harmonics, due to intrinsic dissipation, has been recently provided by [24], under the assumption of various

plastic hardening material models.

Krapez [5] and Bremond [37] were among the first to propose the FH and SH amplitudes as monitoring metrics in the FLTM scheme. In particular, the SH analysis in [37], called D-mode from Dissipation-mode, was also implemented as a software feature in some models of commercial FLIR IR cameras equipped with a lock-in ingress module. More recently, a growing number of authors has adopted the same approach [8, 9, 16, 18, 21, 22]. In particular, some authors have also suggested to use the phase of the FH [9, 20] and the phase of the SH [21, 25], as suitable metrics in the FLTM scheme. Both methodologies are based on the expected phase shift that the first and second harmonic are likely to experience when heat dissipation is gradually introduced by irreversible structural changes.

In the present work, the heat diffusion equation is first recalled highlighting the mechanisms by which both the amplitude and phase of the FH and SH signals may be used as suitable indicators of increasing dissipation. The theoretical discussion is supported by the analysis of experimental data obtained from C45 steel samples subject to uniaxial fatigue cycling with loading ratios of both $R = -1$ and $R = 0.1$.

Special attention is then devoted to the analysis of the phase of the SH. It is observed how this parameter presents a bimodal spatial distribution, whose peaks are well separated by an angle of about 180°. This behavior is explained as the result of two competitive thermomechanical sources, one predicted by the second order thermoelastic theory, and one related to dissipation. It is found that with the increase of the load amplitude, the dissipation source prevails over the thermoelastic source, and the SH phase evolves towards a unimodal distribution.

2. Theoretical background

2.1. Frequency-resolved Thermo-mechanical parameters

The parameters proposed in this study are obtained from the harmonic content of the temperature signal, sampled over a certain time window [30]. In particular, the first harmonic (FH) and second harmonic (SH) are extracted as the components at the loading frequency, f_L, and at twice the loading frequency, $2f_L$.

A correlation of these parameters with the thermomechanical coupling sources can be established by recalling the heat diffusion equation for solid materials. This describes the local thermodynamic status of the system through the following state variables: the temperature T, the strain tensor ε_{ij} and internal state variables $\mathbf{x}$ describing material micro-structural changes. By combining the first and second principles of thermodynamics and introducing the Helmholtz free energy thermodynamic potential, H, it is possible to obtain the local energy balance in the form of a heat diffusion law [35, 38], written in terms of power as follows:

$$\rho C_\varepsilon \dot{T} - k\nabla^2 T = D_m + T\frac{\partial \sigma_{ij}}{\partial T}\dot{\varepsilon}^e_{ij} + T\rho\frac{\partial^2 H}{\partial T \partial \mathbf{x}}\dot{\mathbf{x}} + q_s \tag{1}$$

where:

- $k\nabla^2 T$ accounts for the spatial heat diffusion;
- D_m represents the intrinsic dissipation;
- $T\frac{\partial \sigma_{ij}}{\partial T}\dot{\varepsilon}^e_{ij}$ is the first thermomechanical coupling consisting of the thermoelastic heat source, linked to deformation in the elastic field;
- $T\rho\frac{\partial^2 H}{\partial T \partial \mathbf{x}}\dot{\mathbf{x}}$ represent the internal heat sources related to the other thermomechanical coupling effects associated to the vector of internal variable $\mathbf{x}$;
- q_s takes into account any external heat input.

The transformation can be assumed as adiabatic when the loading frequency exceeds a certain threshold and intrinsic dissipation rates are negligible [6]. This is generally achieved within the purely elastic range, at loading amplitudes sufficiently small to rule out any internal state changes, i.e. $\dot{\mathbf{x}} = \mathbf{0}$. It is also noticed that changes of internal variable are still negligible in elasto-plastic materials subjected to fatigue loads, when temperature variations are reduced and dependence of material state on temperature does not induce coupling heat sources, according to [35, 39]. In this case, the thermoelastic heat source is the only relevant heat source and Eq. (1) ca be rewritten as:

$$\dot{T} = \frac{T}{\rho C_\varepsilon} \frac{\partial \sigma_{ij}}{\partial T} \dot{\varepsilon}^e_{ij} \tag{2}$$

integrating over time yields:

$$\Delta T = \frac{T_o}{\rho C_\varepsilon} \frac{\partial \sigma_{ij}}{\partial T} \Delta \varepsilon_{ij} \tag{3}$$

The derivative of the stress tensor with T in Eq. (3) is computed considering the generalized Hooke's elastic law. Two assumptions can be made about the dependency of the elastic and physical constants on temperature, which lead to two formulations known as first order and second order Thermoelastic laws [40].

In the first order assumption the dependence of all elastic parameters and the coefficient of thermal expansion (CTE) are neglected. Eq. (3) can then be simplified into the following linear relation:

$$\Delta T = \frac{T_o}{\rho C_\varepsilon} (-\gamma \cdot \delta_{ij}) \Delta \varepsilon_{ij} = -\frac{T_o}{\rho C_\varepsilon} \frac{E\alpha}{(1-2\nu)} \Delta \varepsilon_{ii} = -T_o \frac{\alpha}{\rho C_p} \Delta \sigma_{ii} \tag{4}$$

The second order formulation, proposed by Wong et al. [41, 42], also considers the dependency of elastic parameters and of the CTE from T. This leads to a more complex stress metric that can be summarized as:

$$\rho C_\varepsilon \frac{\dot{T}}{T} = -\left[\alpha + \left(\frac{\nu}{E^2}\frac{\partial E}{\partial T} - \frac{1}{E}\frac{\partial \nu}{\partial T}\right)\sigma_I\right]\dot{\sigma}_I + \left[\frac{(1+\nu)}{E^2}\frac{\partial E}{\partial T} - \frac{1}{E}\frac{\partial \nu}{\partial T}\right]\sigma_i \dot{\sigma}_i \tag{5}$$

where $\sigma_I = \sigma_1 + \sigma_2 + \sigma_3$ is the first stress invariant and $\sigma_i = \sigma_1, \sigma_2, \sigma_3$ are the principal stress components. If a one-dimensional stress field is considered where $\sigma_1 = \sigma$, $\sigma_2 = \sigma_3 = 0$, Eq. 5 becomes:

$$\rho C_\varepsilon \frac{\dot{T}}{T} = -\left[\alpha - \frac{1}{E^2}\frac{\partial E}{\partial T}\sigma\right]\dot{\sigma} \tag{6}$$

Fatigue cycling under loading control induces a purely sinusoidal axial stress that can be expressed as: $\sigma = \sigma_m + \sigma_a \sin(\omega t)$, with ω equal to the angular frequency, $\omega = 2\pi f_L$. Then Eq. (2) and (6) become:

$$\Delta T = -T_o K_o \sigma_a \sin(\omega t) \tag{7}$$

$$\Delta T = -T_o \left(K_o - K_1 \sigma_m\right) \sigma_a \sin(\omega t) - T_o K_2 (\sigma_a)^2 \cos(2\omega t) \tag{8}$$

where:

$$K_o = \frac{\alpha}{\rho C_\varepsilon}; K_1 = \frac{1}{\rho C_\varepsilon}\frac{1}{E^2}\frac{\partial E}{\partial T}; K_2 = \frac{1}{\rho C_\varepsilon}\frac{1}{4E^2}\frac{\partial E}{\partial T} \tag{9}$$

Here it is assumed that $(K_0 - K_1\sigma_m) > 0$, and $K_2 < 0$ which is true for most common metals where, $dE/dT < 0$ (some exceptions comprise the case of Shape Memory Alloys) [43, 44]. Moreover, K_o is defined positive. Therefore, to highlight the phase difference between the terms of eqs. (7, 8), these can be written as:

$$\Delta T = |T_o K_o \sigma_a| \sin(\omega t \pm 180^\circ) \tag{10}$$

$$\Delta T = |T_o \left(K_o - K_1 \sigma_m\right) \sigma_a| \sin(\omega t \pm 180^\circ) - |T_o K_2 (\sigma_a)^2| \cos(2\omega t) \tag{11}$$

The heat source term D_m in Eq. (1) accounts for the intrinsic mechanical dissipation. This is given by the difference between the irreversible inelastic energy rate and the stored energy rate related with the internal material status. The term can be written as:

$$D_m = \sigma_{ij}\dot{\varepsilon}_{ij} - \sigma_{ij}\dot{\varepsilon}^e_{ij} - A_x\dot{\mathbf{x}} = \sigma_{ij}\dot{\varepsilon}^p_{ij} - A_x\dot{\mathbf{x}} \tag{12}$$

The integral of the term $\sigma_{ij}\dot{\varepsilon}_{ij}$ over a loading cycle coincides with the hysteresis loop area.

Several authors have tried to quantify D_m and the weight of the terms involved in Eq. (12) [6, 7, 15, 33, 34, 36, 45–47]. In general, it is found that, under low-amplitude loading cycles, actual intrinsic dissipation is usually negligible compared to the thermoelastic heat source [34, 44]. It instead increases with the increase of the load amplitude and with the applied loading frequency [6].

When a certain amount of plastic deformation is involved during each cycle, a heat source related to dissipation is activated twice in the loading cycle [5, 9, 21, 38]. Therefore, the associated temperature harmonic content has a significant component at twice the loading frequency $2f_L$. This concept was introduced in TSA, see e.g. [37, 46], and the evaluation of the Second Harmonic is often referred to as Dissipation-mode or D-mode, since it is clearly correlated to D_m, although cannot be adopted to quantify D_m straightforwardly. This denomination might, though, be misleading since it does not consider the contribution to the second harmonic from the thermoelastic source, as predicted by the second order theory. Following previous works [24, 26, 36] the irreversible heat is produced near each peak and trough of a loading cycle, and the corresponding temperature has a fundamental frequency at $2f_L$. The SH harmonic component of dissipation is here written as:

$$\Delta T_{d2\omega} = -\left|T_d\right|\cos\left(2\omega t\right) = \left|T_d\right|\sin(2\omega t - 90^\circ) \tag{13}$$

It is observed that the exact evolution of dissipated heat within a loading cycle may depend on several factors, and the related temperature is in general irreversibly increasing in a purely adiabatic scenario. This implies that the SH alone is not able to completely quantify the temperature evolution related to plastic dissipation, and higher order harmonics may well be needed to capture the real temperature evolution [48–50].

The above equations indicate that the thermoelastic and dissipation waves also have peculiar phase shifts, that are summarized in Table 2 and schematically

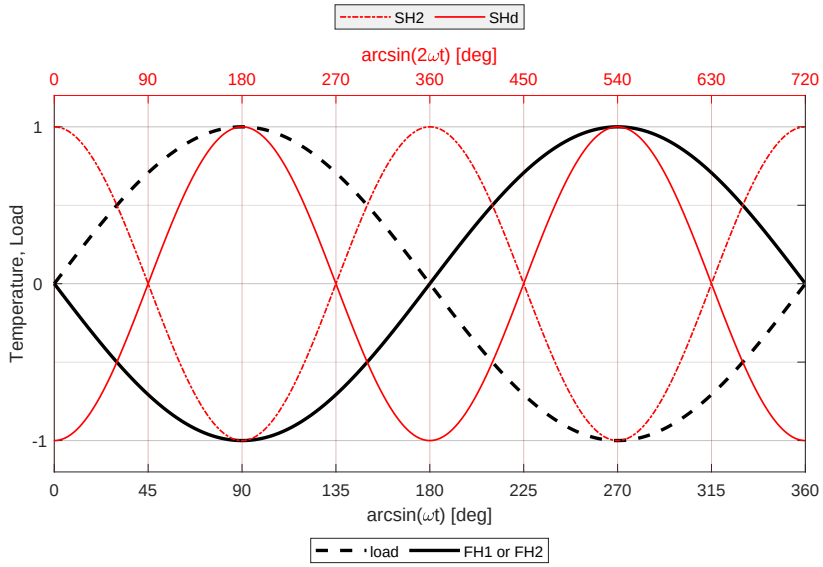

Figure 2: Phase values of the four different signals predicted by the second order thermoelastic effect.

represented in Fig. 2.

Table 2: Relative phase positions of load, thermoelastics and dissipative terms.

Signal component	Time modulation	Phase shift with reference to a pure sine wave	Reference equation
load	$\sin(\omega t)$	$\sin(\omega t)$	
First order FH	$-\sin(\omega t)$	$\sin(\omega t \pm 180°)$	Eqs. (7, 10)
Second order FH	$-\sin(\omega t)$	$\sin(\omega t \pm 180°)$	Eqs. (8,11)
Second order SH	$\cos(2\omega t)$	$\sin(2\omega t + 90°)$	Eqs. (8, 11)
Dissipation SH	$-\cos(2\omega t)$	$\sin(2\omega t - 90°)$	Eq. (13)

Figure 2 provides a comparison of phase differences between the load harmonic, the dissipation fundamental harmonic (Eq. (13)), the first order thermoelastic harmonic, the second order thermoelastic harmonics when $dE/dT <$

0. Figure 2 is a schematic representation of the different phase shifts of the various harmonic terms. The average values are equaled to zero and amplitudes are normalized to one for ease of representation of the phase information. Furthermore, the initial time is synchronized with the pure sine wave, which represents the applied load.

As will be discussed later, this phase representation is not necessarily that retrieved by actual acquired signals, since these can present an initial phase shift that depends on the time of sampling triggering, and is then random and unknown if the triggering is not opportunely synchronized to the applied load.

The relative phase differences between the signals reported in Fig. 2 are those predicted by the thermoelastic models and assumptions described above. It is observed that small departures from these nominal phase positions may arise due to various spurious effects or the relaxing of some of the assumptions at the basis of the thermoelastic theory [5, 9].

2.2. Thermo-mechanical parameters and signal processing

The signal sampled by the IR camera over a time window is processed by means of two procedures: one based on Least-Squares Fitting (LSF) and one on the Discrete Fourier Transform (DFT) [30].

The LSF procedure employed in this work consists of fitting the time resolved signal with the following multiparameter relation:

$$T(t) = T_o + B \cdot t + E\cos(\omega \cdot t - \Phi_E) + D\cos(2\omega \cdot t - \Phi_D) + R\cos(3\omega \cdot t - \Phi_R) \quad (14)$$

where B represents a linear increase of the temperature and ω is the angular frequency of the applied sinusoidal load. A third harmonic term is also introduced to improve the fitting, since this harmonic can also carry a significant amplitude, as revealed by the DFT (see below). A similar expression is used to fit the load signal, that is acquired via the lock-in ingress module of the IR camera.

The harmonic content in terms of amplitude and phase is also obtained by the Discrete Fourier Transform, which is implemented via the *fft* Matlab function [30]. In particular, the parameters extracted by both LSF and DFT are:

- T_o: average temperature of the specimen;
- E: first harmonic amplitude - whitin the linear elastic regime, this coincides with the thermoelastic signal amplitude, and is then expected to be opposite in phase with the applied load, when eq. (4) applies. Some works have found a departure from linearity and a steeper rate of increase as the load amplitude increases and intrinsic dissipation arises [5, 9, 20, 25, 31]. This can be attributed to various effects such as a concurrent increase of the average sample temperature, changes in the material thermoelastic constant, the presence of an important contribution in the first harmonic of the material temperature due to dissipation, when the applied load ratio is $R > 0$;
- D: second harmonic ampltude - this term can be correlated to the second order thermoelastic effect (as evidenced in eq. (5)) and to the dissipated heat (see eq. (13). It can also arise if the applied external load is not a purely mono-frequency wave [21];
- Φ_E: first harmonic phase – changes in this parameter are usually correlated to the onset of damage/plasticization and the concurrent influence on the modulation of the thermoelastic temperature, which may include a retardation with respect to the applied load;
- Φ_D: second harmonic phase - the second harmonic is expected to shift with the progressive onset of dissipation, since the thermoelastic second harmonic, prevailing at low stress amplitudes, is about opposite in phase with respect to the modulated dissipation, that prevails at higher stress amplitudes (see Fig. 2 and section 2.1).

The use of two signal processing procedures in this work allows to avoid some shortcomings of each procedure and to gain more confidence in the output results. In particular, DFT is able to provide the whole harmonic content of the signal at a glance but is prone to errors due to spectral leakage. LSF is insensitive to the spectral leakage error if the loading frequency ω is correctly identified and there is no lack of frames [30]. Furthermore, LSF provides a direct expression of the reconstructed signal and its harmonic waves. In the present work, both LSF and DFT are used in synergy, implementing algorithms for frame drop correction, load frequency identification and spectral leakage minimization. Also, all parameters listed above are processed using in-house developed Matlab® functions that can be applied recursively, within loop structures, to analyze several data in most efficient ways.

The measured harmonic parameters are analyzed according to two different approaches:

- Global: single values of T_o, E, D, Φ_E and Φ_D are averaged over an area (Region of Interest – ROI, see Fig. 3) and thus analyzed to assess if the damage phenomena affect the thermal metrics in a mean sense. The global parameters are usually distinguished by adding a "g" subscript;

- Local: the parameter is analyzed at each pixel, providing the whole field distribution. The maximum variation over the ROI is also retrieved, following the approach proposed in [9]. The 95^{th} percentile is then evaluated, to exclude corrupted values (outliers) in the data processing. The first harmonic phase Φ_E is processed following the Thermoelastic Phase Analysis (TPA) approach proposed in [20].

An example of data analysis performed with the DFT is shown in Fig. 4 for a specimen tested at the loading ratio of $R = -1$ and in Fig. 5 for $R = 0.1$. The features are considered to be representative of all the tests run at both $R = 0.1$ and $R = -1$.

Here, a comparison of the spectrum from three signals is shown. The three signals are: (i) the externally applied load (acquired through the lock-in module

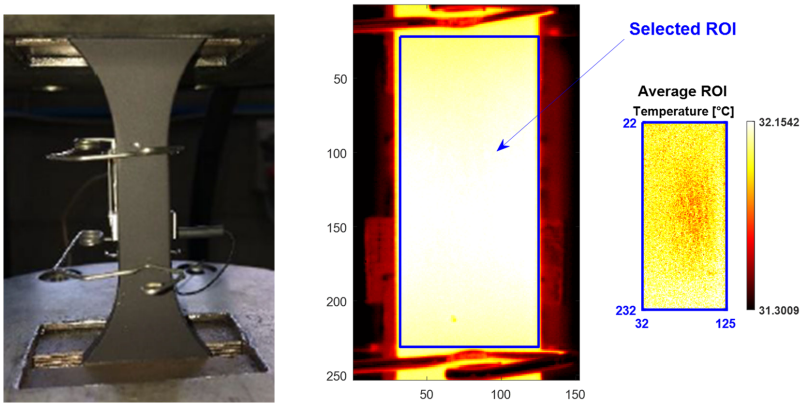

Figure 3: Selected ROIs for the extraction of the phase-signal.

of the IR camera.), (ii) the temperature from a single point located in the center of Region of Interest (ROI) area defined on the sample, (iii) the average temperature over the ROI area (see Fig. 4, 5).

Each power spectrum in Fig. 4 shows some peaks above the noise bed level, which are generally located at the loading frequency and at integer multiple values of the loading frequency. The present analysis has revealed the presence of a harmonic component at twice the loading frequency also in the load power spectrum, suggesting that the second harmonic value in the temperature spectrum could be in part influenced by a thermoelastic response arising from this spurious load harmonic.

The presence of loading harmonics above the fundamental has been reported also by other authors [21, 32] and has been attributed to vibrations transferred by the loading machine. Here it is observed that, if the load cycle includes a zone of marked material non-linearity, and the test is run under load control, then the machine actuator is required to rapidly adjust its rate at specific instants of the load cycle. If the dynamic response of the controller is not fast enough for such changes, this might result in a corruption of the pure mono-frequency loading wave.

Figure 4 shows also that averaging the temperature over a ROI has the effect

of reducing the random noise (lower noise bed). This improves the sensitivity and allows to better distinguish higher harmonics amplitudes from noise.

2.3. Evaluation of harmonics phases

As discussed in section 2.1, one aim of the work is to analyze the relative phase differences of the first and second harmonic components. The LSF is used to evaluate the FH phase of the load signal, Φ_L, by using the same fitting model of eq. (14).

For each test in the stepwise sequence (see Fig. 1a), the phase difference between the load signal and the thermoelastic signal is then obtained as:

$$\Phi_{E_g} - \Phi_{load} \tag{15}$$

The TPA approach [20] is also considered, evaluating the spatial variation of the FH phase within the ROI as:

$$\Delta\Phi_E = \Phi_{95^{th}} - \Phi_{5^{th}} \tag{16}$$

Each acquired sequence of thermograms has an initial FH phase that varies randomly, since no triggered synchronization is used to start the IR camera sampling. To compare the phases of the harmonics from different acquisitions, it is then necessary to eliminate the random component of the phase, and shift all harmonics to a common reference, as done in Fig. 2. To do so, the following procedure is applied:

- The LSF is used to fit the load signal from each acquired sequence (one per each block of constant amplitude loading, see Fig. 1a). The FH term is then obtained whose modulation is described by $\cos(\omega t - \Phi_L)$ (according to eq. (15));
- the load FH is shifted to become: $\cos(\omega t - \Phi_L + \Phi_L) = \cos(\omega t)$;
- The load FH is then further shifted to represent a pure sine wave (according to Fig. 2):$\cos(\omega t - \Phi_L + \Phi_L) = \sin(\omega t)$;

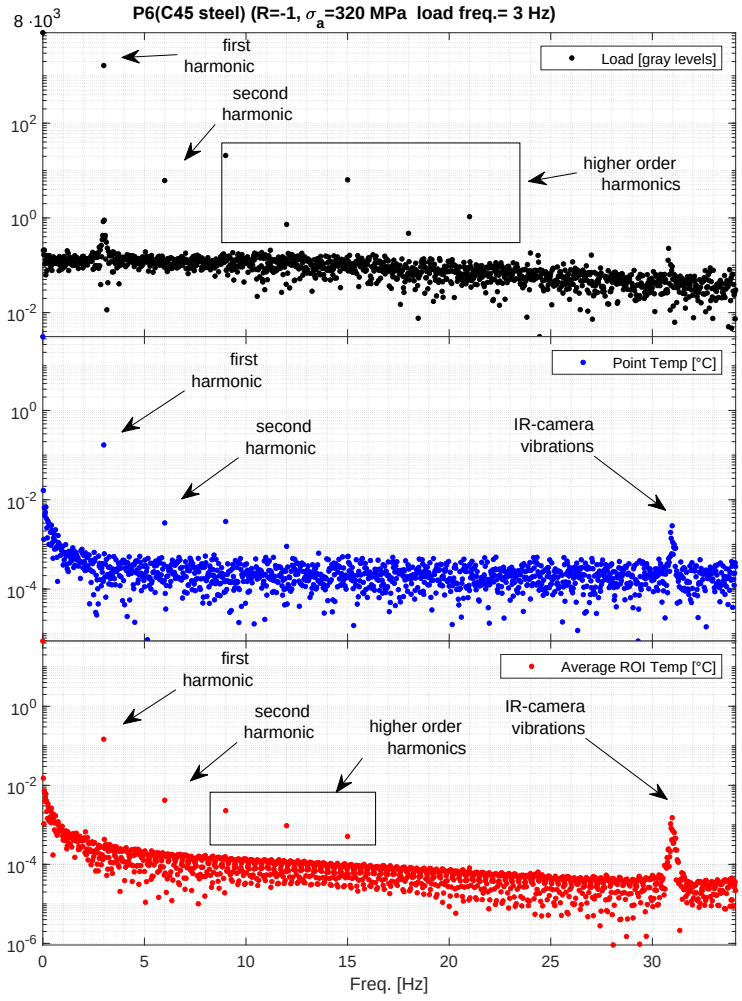

Figure 4: Power spectrums of (i) Load Signal, (ii) Single-Point temperature signal, (iii) Average Temperature signal for a specimen tested at $R = -1$. A logarithmic scale is adopted for the y-axis.

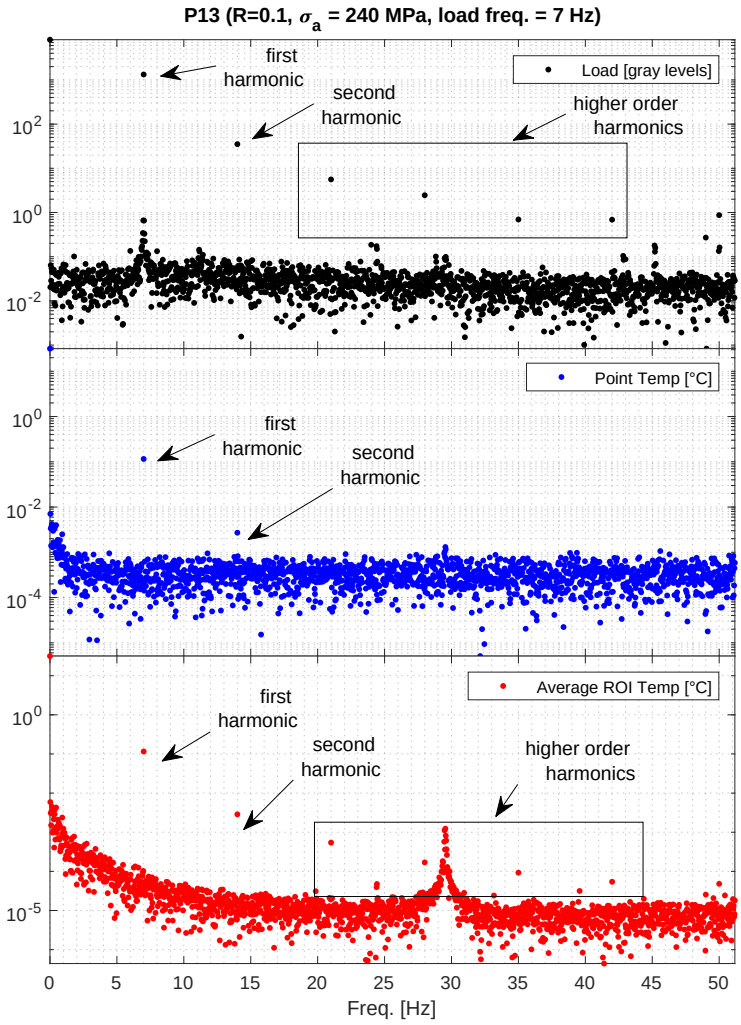

Figure 5: Power spectrums of (i) Load Signal, (ii) Single-Point temperature signal, (iii) Average Temperature signal for a specimen tested at $R = 0$.. A logarithmic scale is adopted for the y-axis.

- The same phase shift applied to the load FH is applied also to the temperature FH: $\cos(\omega t - \Phi_E + \Phi_L - 90°)$;
- The equivalent value of phase shifting for the SH temperature signal is then obtained as: $\cos(2\omega t - \Phi_D + 2\Phi_L - 180°)$.

Summarizing, the following shifts of the phases obtained with the LSF are required, to adhere with the representation of Fig. 2:

$$\begin{aligned} \Phi_{L_{shifted}} &= \Phi_L - \Phi_L + 90° \\ \Phi_{E_{shifted}} &= \Phi_E - \Phi_L + 90° \\ \Phi_{D_{shifted}} &= \Phi_D - 2\Phi_L + 180° \end{aligned} \tag{17}$$

Figure 6 shows an example of such synchronization.

3. Experimental case study and plan of experiments

3.1. Experimental case study: Tensile C45 specimen

In this work, flat tensile dog-bone specimens made from a C45 steel have been tested. The geometry of the specimens is shown in Figure 7, while mechanical properties are: yield strength $\sigma_Y = 453$ MPa, ultimate tensile strength $\sigma_R = 746$ MPa and Young's Modulus $E = 207.7$ GPa.

The surface of each specimen has been first cleaned from oxides and smoothed by grinding with 400 grit and successively 800 grit sandpaper, then cleaned with ethylic alcohol and finally painted with matt black paint to uniform and enhance infrared emissivity.

A cooled-sensor thermal-camera FLIR SC7000 has been used to monitor the surface of the specimen. The IR camera has an InSb sensor, 20 mK of NETD and a 325×256 pixels Field Of View (FOV).

3.2. Plan of Experiments

Step wise fatigue tests were carried out using a Schenck Hydropuls PSA servo-hydraulic testing machine equipped with a 100 kN load cell. During testing, hysteresis cycles were measured by using the signals acquired from the load

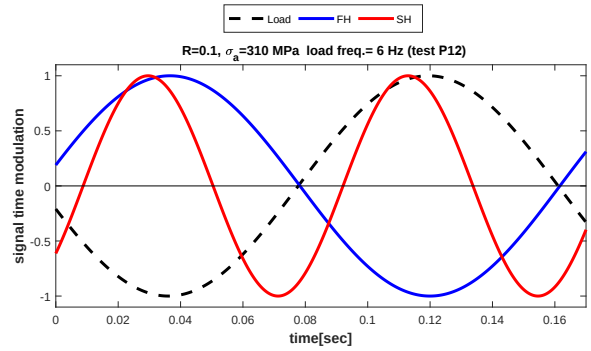

(a)

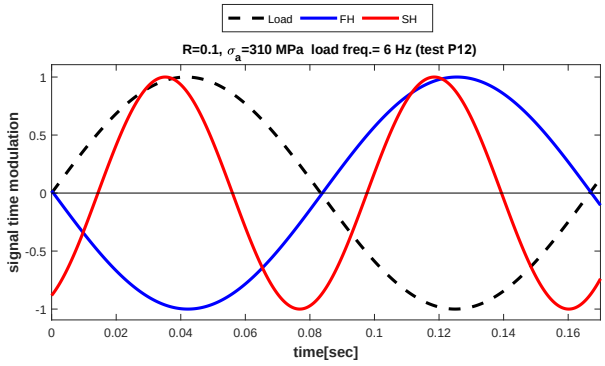

(b)

Figure 6: time modulation plots of load and temperature FH and SH: a) as acquired; b) after the postprocessed shift to syncronise with the load sine wave.

cell and from an MTS extensometer having a gauge length of 25 mm. Each acquisition was started when hysteresis cycles stabilised for the applied stress amplitude and once the thermal equilibrium was reached (plateau stage and constant mean temperature). The sampling frequency of the thermal acquisitions has been set at 204.8 Hz. The obtained spatial resolution of the thermograms is 0.12 mm/pixel ($R = -1$) and 0.13 mm/pixel ($R = 0.1$) and the integration time was set at 1000 μs.

Tests have been conducted following two different loading ratios, $R = -1$ (5 specimens tested) and $R = 0.1$ (4 specimens tested). The acquisitions ranged

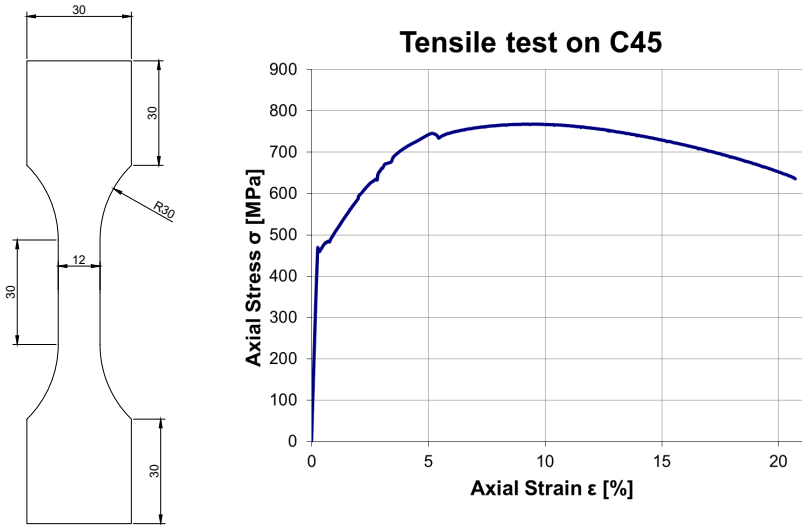

(a) (b)

Figure 7: Geometry of the dog-bone tensile specimens used in the test.

between 10 s (2048 frames) for the specimens tested at the loading ratio of $R = -1$ and 40 s (8192 frames) for $R = 0.1$. The values of applied load and testing frequency changed for every test. The testing parameters are summarized in Tables 3 and 4.

Table 3: Testing parameters for $R = -1$. Written inside the brackets, the number of experimental points available for each stress level.

Loading Ratio	$R = -1$
Tested Specimens	P4 P5 P6 P7 P8
Stress Amplitude	260 (5), 280 (9), 300 (13), 310 (13), 320 (15), 340 (13), 360 (8) MPa
Loading Frequencies	10, 9, 8, 7, 6.5, 6, 5.5, 5, 3, 2.5, 1.5, 1 Hz
Sampling Frequency	204.8 Hz
Time Window	10 s

Table 4: Testing parameters for $R = 0.1$. Written inside the brackets, the number of experimental points available for each stress level.

Loading Ratio	$R = 0.1$
Tested Specimens	P12 P13 P14 P15
Stress Amplitude	150 (5), 170 (8), 190 (8), 210 (8), 230 (8), 250 (7), 270 (8), 290 (9), 310 (7) MPa
Loading Frequencies	15, 12, 11, 10, 9, 8, 7, 6, 5.5, 5, 4.5 Hz
Sampling Frequency	204.8 Hz
Time Window	40 s

4. Results

In this section, results of the following parameters: the average temperature T_o and the harmonic metrics E, Φ_E, D, Φ_D are reported in the form of full field maps and as reduced global or local metrics. In this second case, the curves plotting the harmonic metrics vs load amplitude, also referred to as stepwise plots, consider a value averaged over all tests performed at the same load amplitude. The experimental scatter is then reported by plotting errorbars with size equal to two times the standard deviation ($2\sigma = 95\%$ confidence interval).

Figures 8 - 12 report full-field maps. For the sake of brevity, only the maps obtained for some load levels of one specimen (i.e. P13) are displayed, since they can be considered as representative of the general features observed in all specimens, at both $R = -1$ and $R = 0.1$.

In each map, a green and a blue cross mark are shown on the pixels with values corresponding to the 5^{th} percentile and 95^{th} percentile of the ROI distribution. It is observed that these markers generally change their positions from one test to another, making it difficult to identify a specific location where the monitored parameter is significantly changing with the increase of the load amplitude. This behavior was also observed when taking the $98^{th} - 2^{nd}$ and the

$90^{th} - 10^{th}$ percentile ranges.

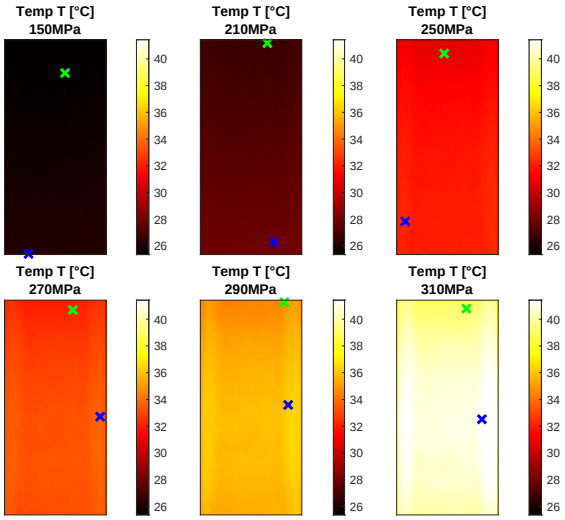

Figure 8: Temperature metric obtained for each analysed test (specimen P13). The green and blue crosses mark respectively the minimum value (5^{th} percentile) the maximum value (95^{th} percentile).

It is reported that the standard deviation of the maps in E and Φ_E is significantly lower than in D and Φ_D, and the phase Φ_E is oscillating around just a few degrees.

It is reported also that the average values of E and Φ_E, calculated from all the points in the ROI, are practically identical to the values of E and Φ_E obtained applying the LSF to the single signal obtained from averaging the temperature over the ROI. This is instead not the case for D and Φ_D, for which some significant differences arise.

4.1. Stepwise plots: T_o

Stepwise plots showing the trend of the average temperature T_o versus σ_a are reported in Fig. 13, for the case of $R = -1$, and Fig. 14 for $R = 0.1$.

It is observed that for both load ratios, the global values (Fig. 13a and Fig. 14a) are very similar to the local values (Fig. 13b, 14b). In this case the global

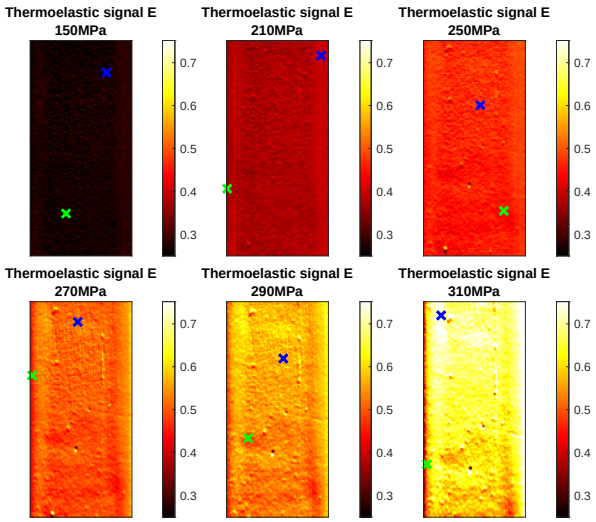

Figure 9: First-Harmonic metric E obtained for each analysed test (specimen P13). The green and blue crosses mark respectively the minimum value (5^{th} percentile) the maximum value (95^{th} percentile).

value is the average temperature and the local value is the the 95^{th} percentile. The similarity of behavior is ultimately due to the low standard deviation of the temperature distribution.

It is also observed that T_o is not subject to steep increases, at least of the order of magnitude reported in other works [2, 4, 18], where the same material is tested. The absence of an abrupt increase of the curve is likely to be attributed to the lower loading frequencies of the higher stress amplitudes applied in this work (see tables 3, 4).

Regarding the case of $R = -1$, there is an initial increase which then evolves towards a plateau after about 310 MPa. The level of scatter at some mid values of σ_a is rather high to identify a clearer trend, and the plateau observed at the higher values of σ_a is most likely due to the lower frequencies applied here.

Regarding the case of $R = 0.1$, a slight deviation from the linearity is noticed after about 210 MPa. In general, the trend is now more regular than the case of $R = -1$, and always increasing. It is also noticed that the deviation from

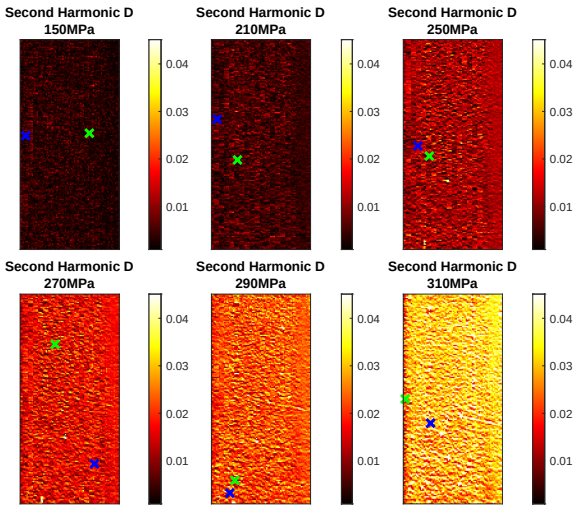

Figure 10: Second-Harmonic metric D obtained for each analysed test (specimen P13). The green and blue crosses mark respectively the minimum value (5^{th} percentile) the maximum value (95^{th} percentile).

linearity coincides with a value of σ_a such to bring the maximum applied stress over the material yield stress. In fact, in the case of $R = 0.1$, the yield stress σ_y is exceeded by values of σ_a higher than $\sigma_y(1-R)/2 \approx 204$ MPa. It is finally observed that the mean temperature measured during all load steps, never exceeds 50°C, as can be seen from Figures 13, 14. These levels of temperature increase are considered too low to influence or modify the room-temperature damage behaviour of the material, or its intrinsic room-temperature structural response in general. As also stated in Section 2.1, at these levels of temperature increase, the dependence of the material state on temperature does not induce coupling heat sources [35, 39].

4.2. Stepwise plots: E

Plots of the first harmonic amplitude E vs σ_a are reported in Figures 15 and 16. Figure 17, shows the hysteresis loops registered during the temperature sampling window for the evaluation of E. These hysteresis loops are stabilised,

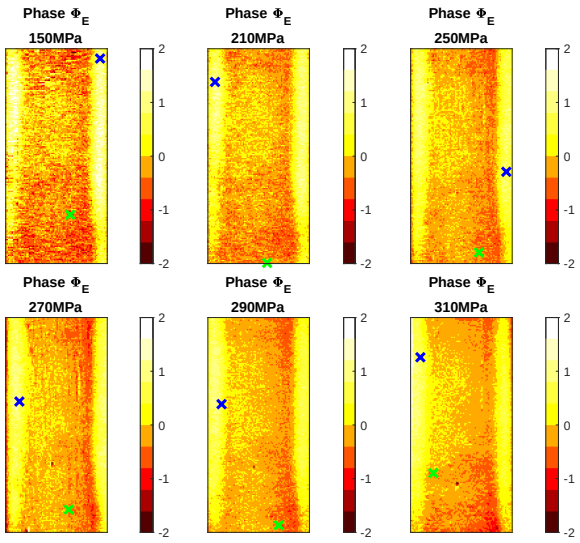

Figure 11: Thermoelastic phase metric Φ_E obtained for each analysed test (specimen P13). The green and blue crosses mark respectively the minimum value (5^{th} percentile) the maximum value (95^{th} percentile).

i.e. the sampling window is started after the increase of the mean and amplitude load of each step has produced its transitory changes on the stress-strain curve. For the case of $R = 0.1$, it is observed a marked mean positive strain accumulation (ratcheting). The sampling window is though started after the stabilisation of the hysteresis loop, and there is no further accumulation of plastic strain during cycling. The thermoelastic signal exhibits a nearly linear behavior, already predicted by the thermoelastic law Eq. (3), when the material is stressed within its linear elastic range. The low fluctuations of values of E over the ROI also explaines the similar behaviour between the average E and the 95^{th} percentile E.

In the case of $R = -1$ the maximum applied stress is 360 MPa, versus a yield stress of 450 MPa. Even if the range is contained within the expected linear elastic zone, it is seen that the stabilised hysteresis loop areas grow with the increase of σ_a (see Fig. 17). This though, does not seem to have a significant

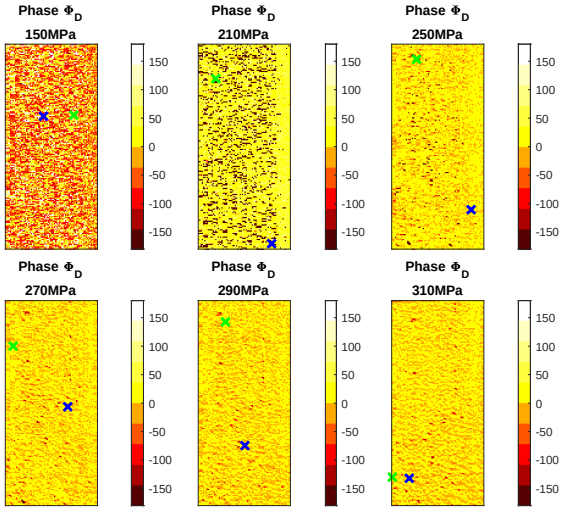

Figure 12: Second harmonic phase metric Φ_D obtained for each analysed test (specimen P13). The green and blue crosses mark respectively the minimum value (5^{th} percentile) the maximum value (95^{th} percentile).

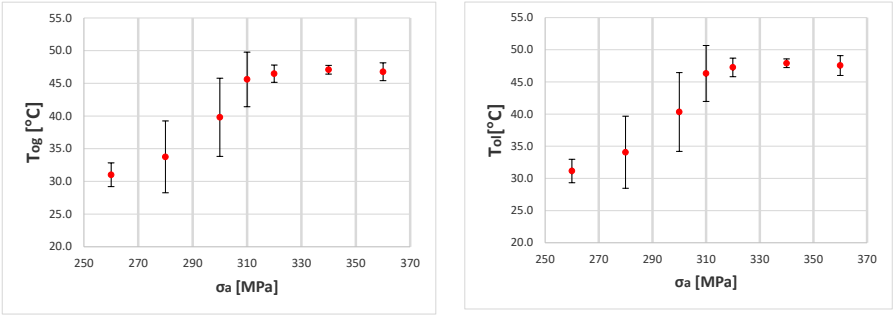

(a) (b)

Figure 13: stepwise plots of the average temperature for $R = -1$. Comparison between the global (a) and local (b) approaches.

impact on the trend of E.

In the case of $R = 0.1$ the yield stress is exceeded by values of σ_a higher than $\sigma_y(1 - R)/2 \approx 204$ MPa. Even so, only a slight deviation from the linear

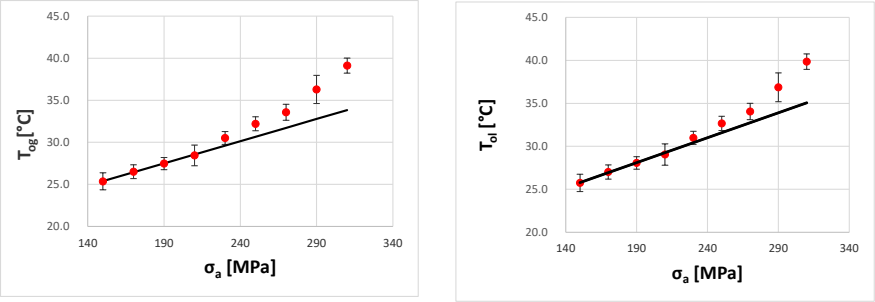

(a) (b)

Figure 14: stepwise plots of the average temperature for $R = 0.1$. Comparison between the global (a) and local (b) approaches.

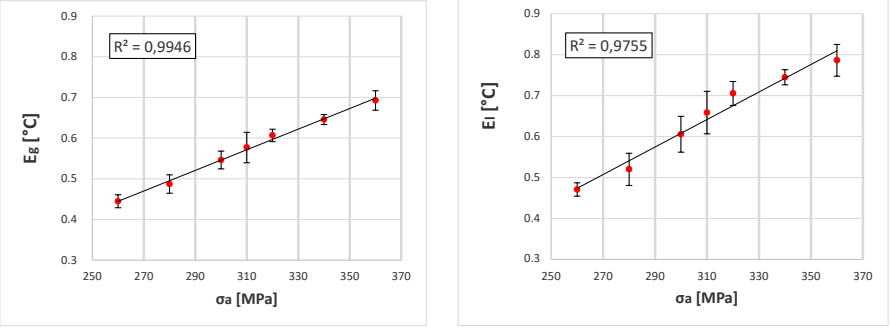

(a) (b)

Figure 15: First harmonic amplitude E for $R = -1$. Comparison between the global (a) and local (b) approaches.

trend of E is observed up to values of $\sigma_a = 320$ MPa. In this case, the material is cycling after it has been hardened in the first cycles, and therefore it is likely to be still working under prevailing linear elastic conditions. This is confirmed by the stabilised hysteresis loops acquired at different σ_a and shown in Fig. 17, which also show a significantly smaller area and exhibit a marked ratcheting [2].

4.3. Stepwise plots: Φ_E

The analysis of the thermoelastic phase with increasing σ_a is reported in Figs. 18, 19.

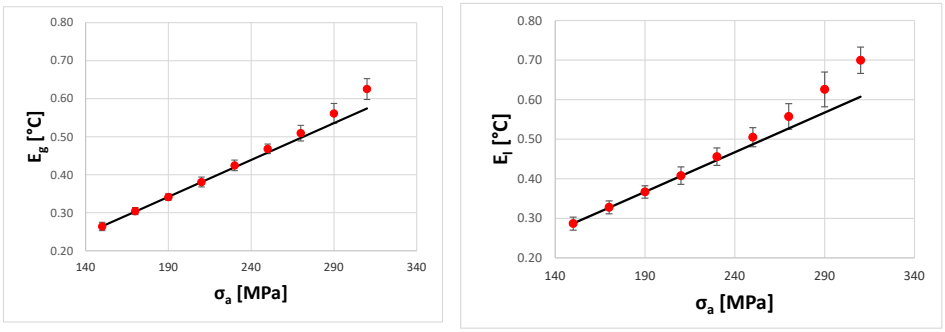

(a) (b)

Figure 16: First harmonic amplitude E for $R = 0.1$. Comparison between the global (a) and local (b) approaches. The continuous black line is a linear regression based on the first three experimental points.

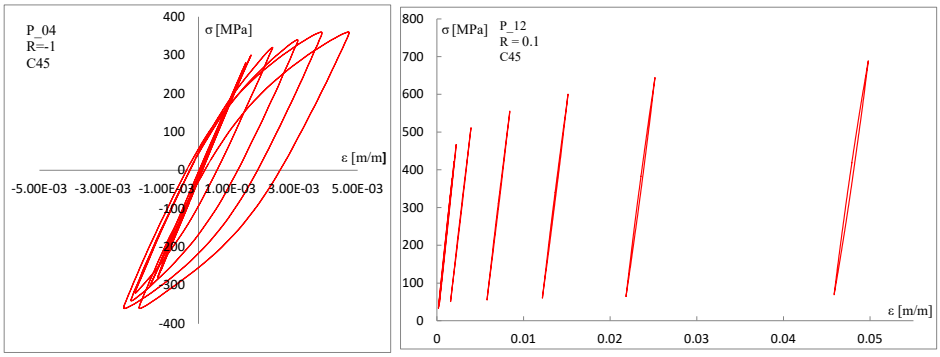

(a) (b)

Figure 17: Examples of stabilised hysteresis loops for increasing σ_a. (a) $R = -1$; (b) $R = 0.1$

The average value of Φ_E over the ROI is first considered and subtracted to the phase of the load FH signal (see also eq (15). For both the cases of $R = -1$ and $R = 0.1$ (Fig. 18a and Fig. 19a), it is found that this phase difference has only small random oscillations around 180°. Therefore, the load signal is always in opposite phase with the FH temperature harmonic. This is in accordance with the Thermoelastic effect laws. It is noteworthy that this behavior is kept unaltered for the whole range of σ_a applied. Therefore, the average thermoelastic phase seems to be little or no sensitive to early fatigue

damage onset.

The analysis of the distribution of the thermoelastic phase over the ROI follows the TPA approach [20], i.e. the difference between the 95^{th} and $5th$ percentile of Φ_E is considered, and results are plotted in Figs. 18b and 19b for $R = -1$ and $R = 0.1$. It is seen that the scatter between different tests is significantly higher than that found in the global approach, but a peculiar trend is still recognized from the average values. Figure 18b shows an increasing trend starting from the third experimental σ_a value (300 MPa). Figure 19b shows a v-shaped trend, with an inversion between 230 and 250 MPa. It is noticed that similar v-shaped trends and similar levels of noise are also reported in [9].

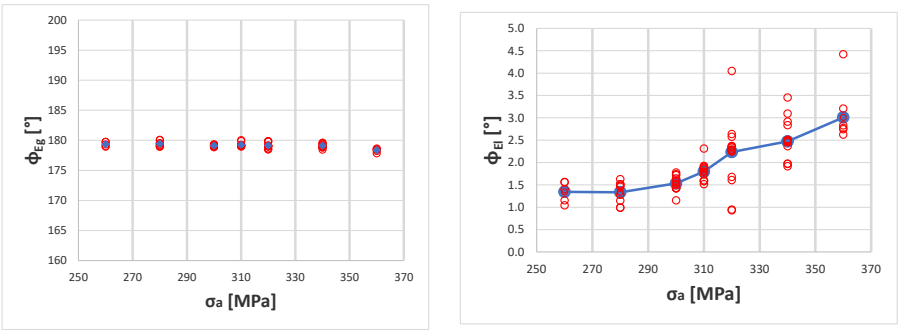

(a) (b)

Figure 18: Thermoelastic phase Φ_E for $R = -1$. Comparison between the global (a) and local (b) approaches. The red dots represent the experimental points, while the blue dots are the mean values.

4.4. Stepwise plots: D

Plots of the second harmonic amplitude D versus σ_a are reported in Figs. 20 and 21. This time, both the global and local approaches show a clear bilinear trend, with a considerable increase between $300 \div 310$ MPa for $R = -1$, and $210 \div 230$ MPa for $R = 0.1$. It is also noticed that the scatter bands are generally smaller, especially in the case of the average values D_g.

Here, the second harmonic amplitude seems to be able to indicate a range of σ_a values where a change in the rate of growth of D is observed, which can be

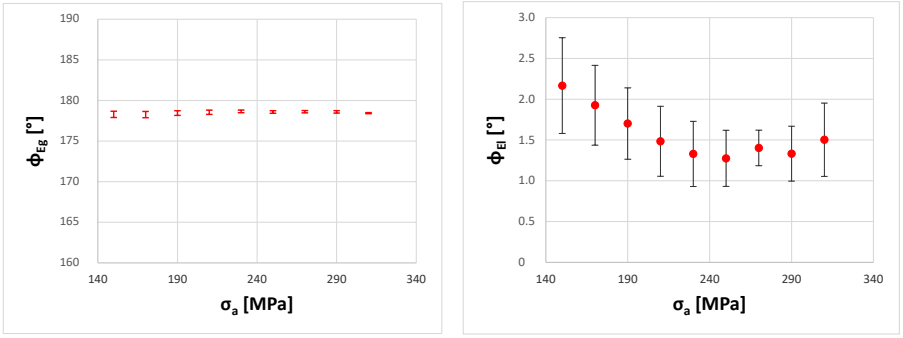

(a) (b)

Figure 19: Thermoelastic phase Φ_E for $R = 0.1$. Comparison between the global (a) and local (b) approaches.

correlated to the material fatigue limit in a typical FLTM approach. A similar threshold range of σ_a can be identified in the stepwise plots of the average temperature T_o (Fig. 13, 14) and thermoelastic phase (Fig. 18, 19).

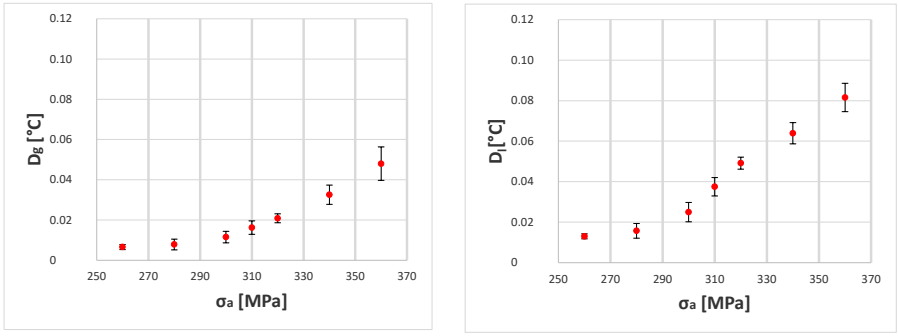

(a) (b)

Figure 20: Second-Harmonic amplitude D for $R = -1$. Comparison between the global (a) and local (b) approaches.

4.5. Evaluation of Φ_D

As observed in Sections 2.2, 2.3 the second harmonic is the result of the combination of three harmonic sources, which are: the thermoelastic component

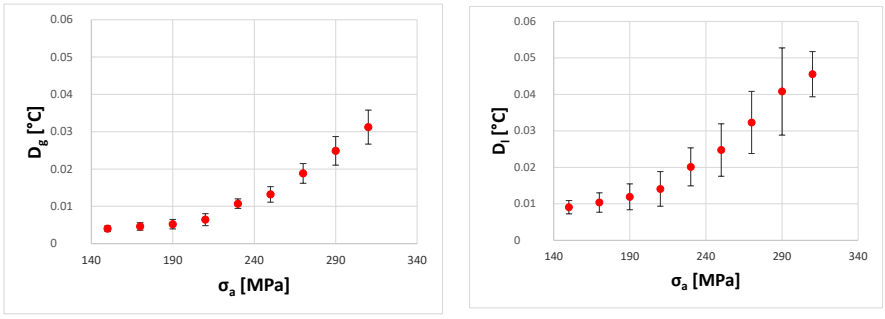

(a) (b)

Figure 21: Second-Harmonic amplitude D for $R = 0.1$. Comparison between the global (a) and local (b) approaches.

revealed by the second order Thermoelastic theory (see eq. (6)), the first order thermoelastic component that is generated in response to the spurious SH of the load (see Fig. 4) and finally the component related to the modulation of intrinsic dissipation within the loading cycle (see Eq. (13) and Fig. 2).

Each of these harmonics is expected to have a different phase shift. In particular, the second order thermoelastic term and the dissipation term are modulated as outlined in Fig. 2. The phase Φ_D measured in this work has evidenced a peculiar behavior i.e. it shows a bimodal distribution over the ROI, that is more evident at lower values of σ_a and gradually evolves towards a narrower unimodal distribution at the higher values of σ_a. Figure 22 shows some maps of Φ_D that evidences the evolution of the distribution from initial bimodal to final unimodal.

Figures 23, 24 report an example of histograms of the distribution of angles over the ROI, for a sample tested at $R = -1$ and one at $R = 0.1$.

Figures 23, 24(left-column) report histograms of the density distribution of values of Φ_D measured over the ROI. The x-axis reports Φ_D after synchronization (see section 2.2 and eqs. (17)), while the y-axis shows the number of occurrences for intervals of Φ_D of 10° width. Therefore, angles closer to +90° are believed to be correlated with the second order thermoelastic component

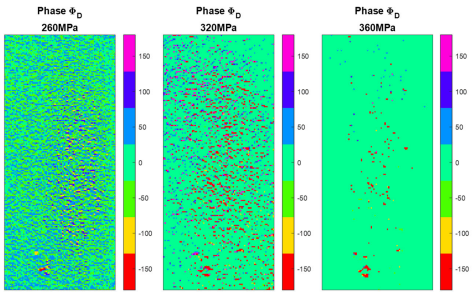

Figure 22: Second-Harmonic phase evolution Φ_D for $R = -1$ at different load levels. As the load increases, the phase becomes more uniform.

and angles closer $-90°$ agree better with the expected position of the intrinsic dissipation wave.

Figures 23, 24(right-column) plots the corresponding harmonic waves. In particular, four curves are reported: the load and the E curve, that are found to be opposite in phase to each other, and two red curves with two different line types. The continuous red curve corresponds to the higher peak of the adjacent histogram on the left column. The dotted red curve corresponds to the lower peak of the histogram.

It is reported that the application of the motion compensation tool from the FLIR software, compensating for the relative movement of the sample points and the sensor pixels due to deformation, does not change the behavior described in Figures 23, 24. All samples at both $R = -1$ and $R = 0.1$ show very clearly the transition from a marked bimodal to a marked unimodal distribution of values of Φ_D, with unimodal angle at higher stress amplitudes σ_a always approaching the position expected for a dissipative behavior, i.e. $\Phi_D = -90°$.

It is interesting to report also stepwise plots of the average Φ_D vs σ_a, as done with the previous metrics. In this case though, averaging the values of Φ_D over the ROI would mean averaging values of points exhibiting two physically different behaviors. Therefore, the result of averaging would lose the physical meaning and would yield a value that somewhat depends on the relative bimodal distribution and on which physical effect is prevailing at a given load amplitude.

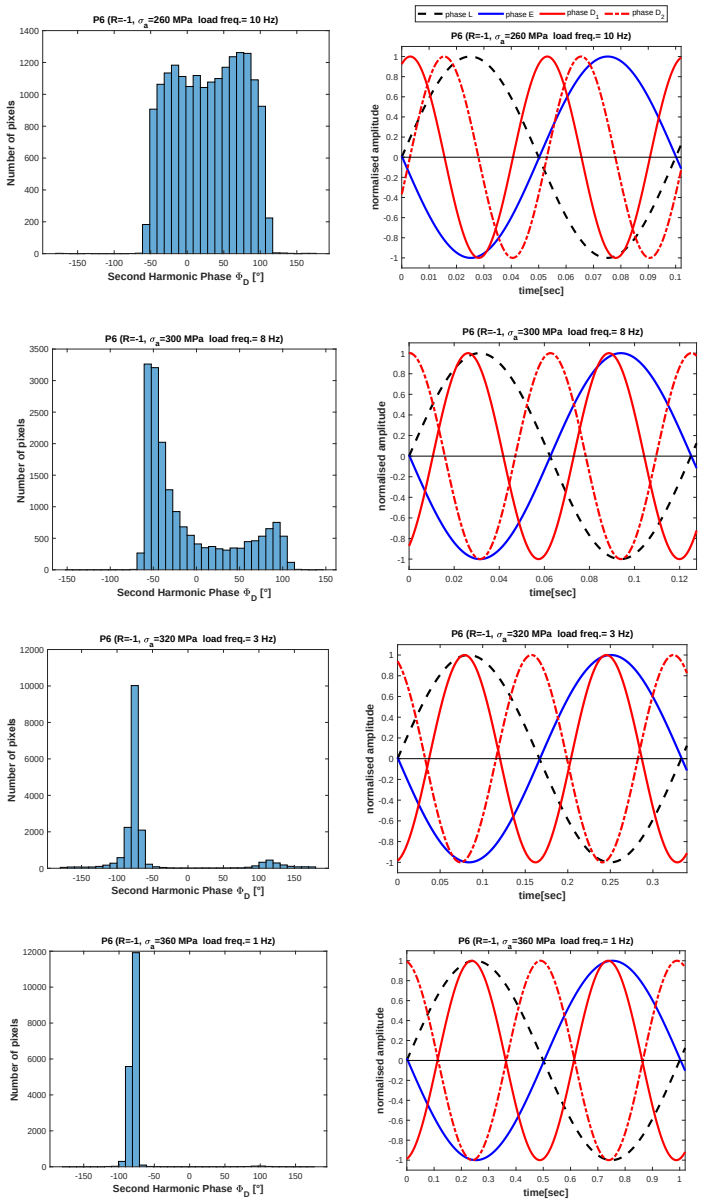

Figure 23: Case $R = -1$. Left column) histograms of the number of pixels in the ROI versus the Φ_D angle synchronized with the sine wave. Right Column) Representation of phase modulation according to Figs 2 and 6.

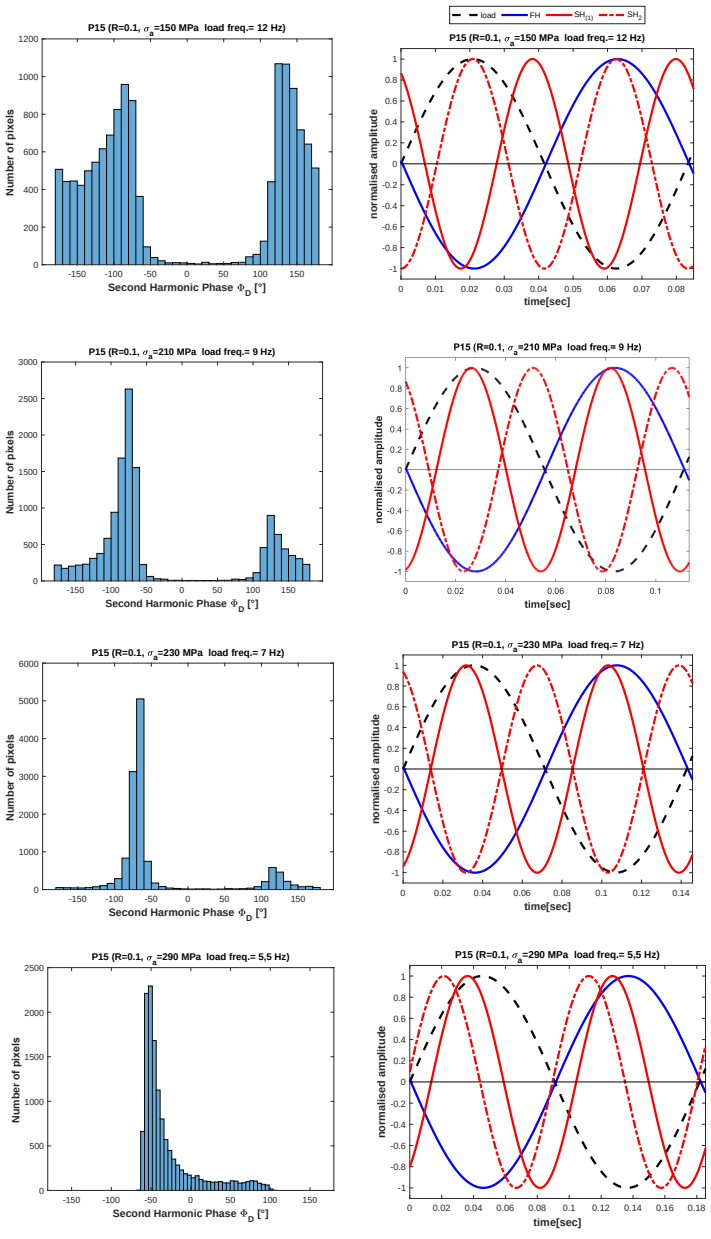

Figure 24: Case $R = 0.1$. Left column) histograms of the number of pixels in the ROI versus the Φ_D angle synchronized with the sine wave. Right Column) Representation of phase modulation according to Figs 2 and 6

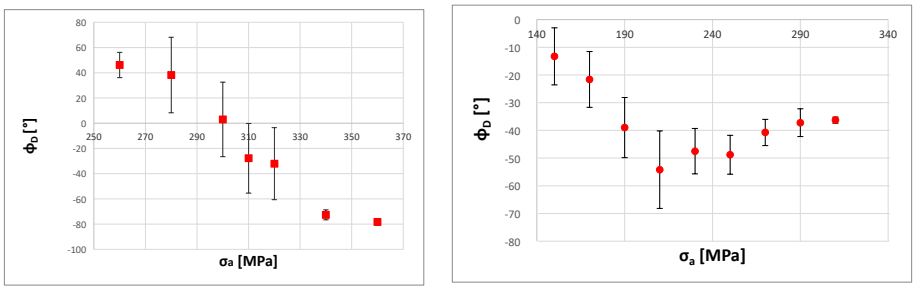

(a) (b)

Figure 25: plots of the ROI averaged Φ_D versus σ_a for: a) $R = -1$; b) $R = 0.1$.

Figure 25 shows such stepwise plots. The plots are still able to identify the transition towards the onset of high dissipation, which happens at values of σ_a that are in good agreement with those found for the other metrics, T_o, D, Φ_E. It is found that the scatter band is rather high in the transition zones. This is due to both the inclusion of different samples and on the bimodal behavior, which determine a strong fluctuation of the average value. Nevertheless, as the load amplitude increases, the scatter is significantly narrowed, due to a progressively prevailing of the dissipation behavior.

5. Discussion of results

As described in Section 2.1, E, D, Φ_E and Φ_D describe the peculiar temperature modulation induced by the thermoelastic heat source. Section 2.2 has illustrated the data processing methodology implemented to extract the above parameters. The fact that the temperature has meaningful harmonic content at the load frequency (first harmonic) and twice the loading frequency (second harmonic) is explained by the thermoelastic heat source, as outlined in Section 2.1. The rise of a dissipative heat source is able to further modify the temperature modulation. Section 4 has presented the trends of the harmonic parameters (E, D, Φ_E, Φ_D) versus the applied stress amplitude (i.e. the stepwise plots). The rising of heat dissipation sources introduces some anomalies on the measured thermoelastic behaviour. Therefore, as stated in the Introduction section,

the above mentioned frequency domain parameters may provide a signature of the rise of heat dissipation sources that some authors have also identified as an early indication of a fatigue limit threshold [2, 5, 9, 10]. In this section the maps and trends of the four parameters E, D, Φ_E, Φ_D are further commented analyzing their ability to indicate the early onset of material degradation and discussing some related issues. The rising of heat dissipation sources introduces some anomalies on the measured thermoelastic behaviour.

5.1. Local vs Global approach

Since high-cycle fatigue involves the enucleation and propagation of a macroscopic crack at a local site, one would assume that the early estimation of the fatigue limit requires the identification of a specific location where the crack is being enucleated. Therefore, the harmonic metrics should be measured in the whole field of potential crack enucleation and analyzed in terms of spatial distribution. It can be argued, though, that if a rapid fatigue limit estimation is sought, the number of applied cycles might not be sufficient to identify a clear and unique location of crack onset.

It is observed that works in the literature which have analyzed thermoelastic metrics within a FLTM approach, most often do not report if these metrics are referred to local values or are spatially averaged [2, 5, 22].

In the present work, the local and global definitions of the harmonic metrics and the comparison of maps with indication of the upper and lower percentiles are intended to verify if the onset of dissipation is related to local rather than diffused phenomena.

It is pointed out that also some other authors, e.g. [15], have tried to identify the nature of the heat sources in the early stages of fatigue at low stress levels, and suggested that the earlier irreversible degradation, generally associated with micro-plasticity, is a spread and not localized phenomenon. It is reported that none of the analysed full field maps at any load step have shown evidence of the enucleation of a local surface or subsurface crack. This also considering that parameters such as E are very sensitive at identifying stress concentrations at

crack tips [30].

Plots in figures 13 - 21, relative to both local and global approaches, show similar results and behaviors for the parameters T_o, E, D. It is noticed that the error-bars associated to the monitored parameters are generally narrower in the case of the global approach, since the procedure of averaging is able to reduce the random noise in the experimental data. It is also observed that the 95^{th} percentile pixels identified in the full-field maps generally indicate different locations with the progression of the stepwise tests, thus failing to identify in a consistent way a specific location of damage densification.

In this work, a strong evidence that the detected dissipation originates in clusters of several sparsely distributed zones is provided by the maps of the SH phase Φ_D. As shown before (subsection 4.5), not only Φ_D has a bimodal distribution evolving towards a fully dissipating unimodal map, but also the distribution of "dissipating" clusters and "thermoelastic" clusters seems to be spread uniformly, with little indication of a zone where the dissipating behavior is gathering and localizing.

With regards to the thermoelastic phase Φ_E, the global approach does not seem to be sensitive to the onset of damage or dissipation, and the phase shift of $180°$ with respect to the load signal is pretty much maintained within a narrow scatter band. When the TPA approach is employed, a bilinear trend in the stepwise plots is still recognized, but data in this work appear to be very noisy. This might be due to the gradual decrease of the loading frequency at high σ_a.

5.2. Factors influencing the first harmonic amplitude

Results show that the FH amplitude E does not exhibit a pronounced deviation from the linear behavior, as predicted by the thermoelastic law. This is so for both global averaged and local E values. It is interesting to compare this finding with those available in the literature, in terms of curves of E vs σ_a.

Boulanger et al. [6] have carried out tests on a dual phase DP60 steel tested at both $R = -1$ and $R = 0.1$, and relatively a low frequency of 1 Hz. Their results of the trend of thermoelastic signal show no loss of linearity, even after

some slight plastic hardening. Krapez [5] tested a steel and an aluminum alloy at both $R = -1$ and $R = 0.1$ and frequency of 2 Hz, reporting only slight deviations from linearity, which were better evidenced by plotting in terms of residuals. Urbanek [22] tested some steels at $R = 0$ and at 5 Hz and deviation from initial linearity is still only slight, and of similar extent to that reported in [5]. It is added here that both [5] and [22] do not report information on the contemporary evolution of the sample mean temperature. Colombo et al. [2] tested the same C45 steel investigated in this work, carrying out tests at $R = -1$, 0.1 and 0.5, at the relatively higher frequency of 15 Hz. For the case of $R = -1$, the work reports a marked deviation from linearity of E with growing σ_a, as well as a concurrent marked increase of the sample mean temperature T_o. At increasing R ratio, the deviation from linearity of E and the increase of T_o are gradually and significantly attenuated.

These literature results suggest that a significant role in the behavior of E is likely played by the mean temperature currently achieved by the sample. The same thermoelastic law clearly indicates that the temperature change is proportional to T_o. It is well known that the temperature increase per cycle is higher at higher stress amplitudes [15]. Therefore, if a tensile test is launched at higher loading frequency, the rate of temperature increase is higher, and the sample may reach higher temperatures. A simple calculation of the sensitivity of the thermoelastic signal to the increase of T_o is reported in Appendix A, obtained by using the linear thermoelastic law (eq. (4)) and assuming different scenarios of T_o increase rates.

In the present work there is only a limited increase of mean temperature T_o (see Figs. 13, 14). This is likely due to the gradual decrease of loading frequency with the applied stress amplitude. It is also observed that the increase is higher for the $R = -1$ case and more gradual for the $R = 0.1$ case. This is probably related with the higher hysteresis area achieved in $R = -1$, due to the inversion of strains in each cycle.

In order to consider the influence of T_o changes in the predicted temperature change due to the thermoelastic effect, $\Delta T_{th} = T_o Ko \Delta\sigma$, Figure 26 reports

the values of the ratio $E/\Delta T_{th}$. The thermoelastic constant used here, K_o, is obtained from the linear regression of E versus $T_o\Delta\sigma$ considering only the first three lower values of σ_a, while T_o is the actual value of the sample mean temperature at each test, and therefore varies with σ_a and with the sample.

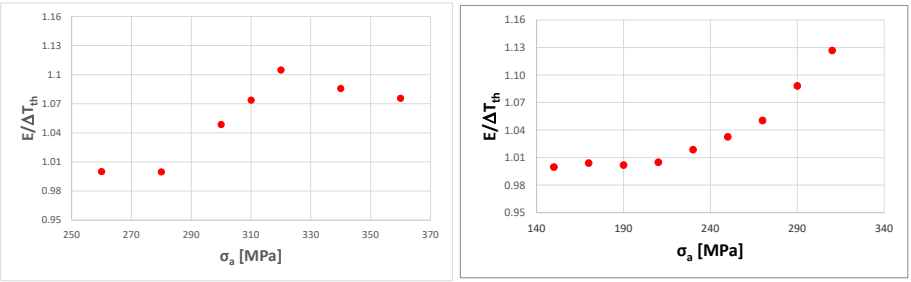

(a) (b)

Figure 26: Plot of $E/\Delta T_{th}$ a) Load Ratio $R = -1$; b) Load Ratio $R = 0.1$.

Results in Fig. 26 provide an estimation of the departure of the measured E from the value of ΔT_{th}. For $R = -1$, it is observed that data do not follow a clear trend, while for $R = 0.1$, the ratio $E/\Delta T_{th}$ is gradually increasing from values of σ_a higher than 190 MPa.

The reason for the increase of $E/\Delta T_{th}$ at $R = 0.1$ could be either an increase of the material thermoelastic constant K_o, or the presence of a first harmonic component in the modulation of heat dissipation, which adds up to the thermoelastic component. It is noticed that during tests at $R = 0.1$ and at high stress amplitudes, the material exceeds its yield point, even if the hysteresis loops remain narrow (see Fig. 26). It is then possible that changes in the microstructure, induced by plastic hardening, might produce some changes in the physical parameters affecting the thermoelastic constant. This is for instance suggested and observed in [27]. Therefore, a potential influence of a change in the material thermoelastic constant cannot be ruled out, even though it is hard to justify a change of more than 10% of K_o due to only plastic flow and hardening.

The presence of a heat dissipation modulated at the FH is instead a plausible

event for tests at $R \geq 0$, and a metric such as $E/\Delta T_{th}$ where ΔT is the measured FH amplitude and ΔT_{th} the thermoelastic amplitude based on the actual T_o and on the thermoelastic constant retrieved from the first data at lower σ_a, could turn out to be an effective parameter to detect the onset of heat dissipation.

5.3. Influence of the 2ω loading component on the D parameter

A noteworthy outcome from analysing the harmonic content of the applied external load is the presence of a second-harmonic component, e.g. Fig. 4.

This might induce also a first order thermoelastic response at the 2ω frequency that would overlap with the already mentioned second order thermoelastic and dissipative sources. If this 2ω thermoelastic component is assumed to follow the first order linear thermoelastic law (Eq. 4) and is denominated E_{2L}, the amplitude of this component can be evaluated by means of the simple proportional relationship:

$$E_{2L} = E \cdot \frac{L_{2\omega}}{L_{\omega}} \tag{18}$$

where $L_{2\omega}$ is the harmonic amplitude of the load signal at the frequency 2ω.

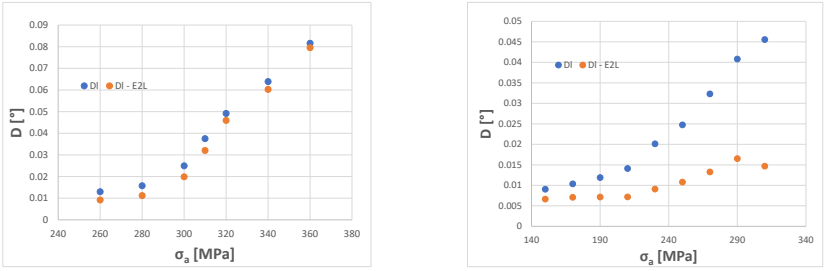

(a) (b)

Figure 27: Second-Harmonic amplitude D, with the subtraction of the 2ω thermoelastic component, E_{2L}. $R = -1$ (a) $R = 0.1$ (b)

Figure 27 shows the trend of D vs σ_a with and without subtracting the calculated E_{2L} aliquot. It is first observed that the correction is pretty constant

in the first part of the plot, before the change of rate increase. In the second part of the plots, the correction appears to be more relevant for the case of $R = 0.1$, Fig. 27b. Since the second-harmonic amplitude is strictly linked to heat dissipation, the bigger size of the hysteresis loops in specimens tested at $R = -1$ (Fig. 17) might justify why the thermoelastic response to $L_{2\omega}$ has a smaller influence, and a more prominent influence in the $R = 0.1$ case.

It is anyway warned that the simple subtraction of the E_{2L} component from the whole SH amplitude would apply only if all the second harmonic heat sources are in phase with each other. This is by no means assured, since the 2ω load wave may have a random phase, which in part depends on the nature of the loading machine employed.

Moreover, as mentioned in Section 5.2, it is likely that at $R = 0.1$ there is some heat dissipation affecting the first harmonic amplitude E at higher stress amplituedes. This would imply that the real thermoelastic amplitude is lower than the one measured, and therefore the value of E_{2L} from eq. (18) might be overestimated.

5.4. Behavior of the Second Harmonic phase

A significant outcome of this work has regarded the analysis of the phase of the SH, Φ_D. Two antagonistic mechanisms are identified which produce a different shift of Φ_D with reference to the applied load. If dissipation is absent or small, as is the case with low σ_a, than the prevailing influence should come from the thermoelastic 2ω component as predicted by the second order thermoelastic theory. As σ_a grows and the material starts to develop significant intrinsic dissipation, then Φ_D is expected to shift towards the peak and trough of the applied load.

At low σ_a results have evidenced a coexistence of both phase shifts values, with a bimodal distribution and a uniform dispersion of points following one or the other behavior (see section 4.5). As σ_a increases, the material clearly migrates towards a unimodal behavior coinciding with a fully dissipating scenario.

It is also observed that the thermoelastic and dissipation phase angles may

deviate from their expected nominal positions. A possible cause for these shifts has been identified in the influence of the spurious SH component of the load, also observed in [21]. In a recent work [24], it is also shown that the peak of the dissipating temperature signal, T_d, may change due to the influence of harmonics higher than 2ω. Therefore, D is only one of many harmonic components composing the T_d signal, and as such, it may be close but not perfectly aligned to the peaks and troughs of the load.

5.5. Agreement with other FLTMs

The samples tested in this work belong to a unique production lot of samples, tested by different research groups from Italian universities. This extended experimental campaign, which is coordinated through the AIAS association (Associazione Italiana Analisi delle Sollecitazioni), has been carried out with the purpose to evaluate different Fatigue-Limit Thermographic Methods, FLTMs, and their reproducibility in different laboratories [2, 8, 11, 28, 33].

In the present work all the discussed metrics indicate a fatigue limit positioned between $300 \div 310$ MPa for $R = -1$, and $190 \div 200$ for $R = 0.1$. These ranges agree well with those published [2], and relative to other FLTMs, some of which also employ thermoelastic parameters [5, 9, 20, 25, 31].

6. Conclusions

In this work uniaxial specimens made of C45 steel have been tested under cyclic, sinusoidal, loading. A number of thermographic metrics have been evaluated at each of a series of blocks having increasing stress amplitude with load ratios of $R = -1$ and $R = 0.1$ (stepwise procedure).

The work has in particular focused on the evaluation of amplitude and phase of the first and second harmonics of the temperature, respectively corresponding with the load frequency and twice the load frequency.

The four different thermal harmonic metrics: E, D, Φ_E, Φ_D have been investigated in order to assess their ability to reveal the onset of damage and heat dissipation.

Some original conclusions have been derived from the performed analysis, which are summarized as follows:

- The E metric shows a dependence on the increase of average temperature and on changes of the thermoelastic constant related to plasticization phenomena.
- The Second Harmonic amplitude D is confirmed to have a good sensitivity to dissipation.
- The analysis of the D and E metrics following the global and local approaches leads to analogous results. This suggests that a specific site of damage concentration is not precisely located.
- The global Φ_E is not sensitive to the dissipative phenomena, since the thermoelastic response is always in opposite phase with respect to the load, also when dissipation is high. Relative changes of the thermoelastic phase are instead found according with the TPA method [20].
- The phase of the SH Φ_D appears to be affected by two effects: a second order thermoelastic effect, that prevails when dissipation is low, and the influence of intrinsic dissipation. These antagonistic phenomena produce a bimodal distribution in the phase maps, characterized by a nominal 180° phase shift between the peaks.

References

[1] "ASTM standard. standard practice for statistical analysis of linear or linearized stress-life (s-n) and strain-life (e-n) fatigue data," *ASTM Stand E739-102015, Annu B ASTM Stand West Conshohocken, PA ASTM Int 2015*, vol. 5, pp. 1–7, 2015.

[2] C. Colombo, M. Sansone, L. Patriarca, and L. Vergani, "Rapid estimation of fatigue limit for C45 steel by thermography and digital image correlation," *Journal of Strain Analysis for Engineering Design*, 2020.

[3] M. P. Luong, "Fatigue limit evaluation of metals using an infrared thermographic technique," *Mechanics of materials*, vol. 28, no. 1-4, pp. 155–163, 1998.

[4] G. La Rosa and A. Risitano, "Thermographic methodology for rapid determination of the fatigue limit of materials and mechanical components," *International Journal of Fatigue*, vol. 22, no. 1, pp. 65–73, 2000.

[5] J. Krapez, D. Pacou, and G. Gardette, "Lock-in thermography and fatigue limit of metals," *Quant Infrared Thermogr*, vol. 5, pp. 277–282, 2000.

[6] T. Boulanger, A. Chrysochoos, C. Mabru, and A. Galtier, "Calorimetric analysis of dissipative and thermoelastic effects associated with the fatigue behavior of steels," *International Journal of Fatigue*, vol. 26, no. 3, pp. 221–229, 2004.

[7] G. Meneghetti, "Analysis of the fatigue strength of a stainless steel based on the energy dissipation," *International Journal of Fatigue*, vol. 29, no. 1, pp. 81–94, 2007.

[8] C. Colombo and L. Vergani, "Thermographic applications for the rapid estimation of fatigue limit," *Procedia Structural Integrity*, vol. 24, pp. 658–666, 2019.

[9] R. De Finis, D. Palumbo, and U. Galietti, "A multianalysis thermography-based approach for fatigue and damage investigations of ASTM A182 F6NM steel at two stress ratios," *Fatigue & Fracture of Engineering Materials & Structures*, vol. 42, no. 1, pp. 267–283, 2019.

[10] M. Ricotta, G. Meneghetti, B. Atzori, G. Risitano, and A. Risitano, "Comparison of experimental thermal methods for the fatigue limit evaluation of a stainless steel," *Metals*, vol. 9, no. 6, 2019.

[11] F. Giudice, G. La Rosa, G. Fargione, and R. Barbagallo, "Fatigue limit assessment by energetic analyses in static and cyclic tensile tests," *Procedia Structural Integrity*, vol. 24, pp. 706–711, 2019.

[12] S. Guo, X. Liu, H. Zhang, Z. Yan, Z. Zhang, and H. Fang, "Thermographic study of az31b magnesium alloy under cyclic loading: Temperature evolution analysis and fatigue limit estimation," *Materials*, vol. 13, no. 22, p. 5209, 2020.

[13] P. Corigliano, F. Cucinotta, E. Guglielmino, G. Risitano, and D. Santonocito, "Fatigue assessment of a marine structural steel and comparison with Thermographic Method and Static Thermographic Method," *Fatigue and Fracture of Engineering Materials and Structures*, vol. 43, no. 4, pp. 734–743, 2020.

[14] A. Lipski, "Change of Specimen Temperature during the Monotonic Tensile Test and Correlation between the Yield Strength and Thermoelasto-Plastic Limit Stress on the Example of Aluminum Alloys," *Materials*, vol. 14, no. 1, 2021.

[15] F. Maquin and F. Pierron, "Heat dissipation measurements in low stress cyclic loading of metallic materials: From internal friction to microplasticity," *Mechanics of Materials*, vol. 41, no. 8, pp. 928–942, 2009.

[16] C. Colombo, L. Vergani, and M. Burman, "Static and fatigue characterisation of new basalt fibre reinforced composites," *Composite Structures*, vol. 94, pp. 1165–1174, feb 2012.

[17] A. Risitano and G. Risitano, "Determining fatigue limits with thermal analysis of static traction tests," *Fatigue & Fracture of Engineering Materials & Structures*, vol. 36, no. 7, pp. 631–639, 2013.

[18] R. De Finis, D. Palumbo, F. Ancona, and U. Galietti, "Fatigue limit evaluation of various martensitic stainless steels with new robust thermographic data analysis," *International Journal of Fatigue*, vol. 74, pp. 88–96, may 2015.

[19] Q. Guo, X. Guo, J. Fan, R. Syed, and C. Wu, "An energy method for rapid

evaluation of high-cycle fatigue parameters based on intrinsic dissipation," *International Journal of Fatigue*, vol. 80, pp. 136–144, 2015.

[20] D. Palumbo and U. Galietti, "Thermoelastic Phase Analysis (TPA): a new method for fatigue behaviour analysis of steels," *Fatigue & Fracture of Engineering Materials & Structures*, vol. 40, no. 4, pp. 523–534, 2017.

[21] D. Shiozawa, T. Inagawa, T. Washio, and T. Sakagami, "Accuracy improvement in dissipated energy measurement by using phase information," *Measurement Science and Technology*, vol. 28, no. 4, p. 044004, 2017.

[22] R. Urbanek and J. Bär, "Evaluation of the Thermo-Elastic Behavior of a High-alloyed Steel by Fourier Transformation based Lock-In-Thermography," in *Proceedings of QIRT 2018, 14th Quantitative InfraRed Thermography Conference, 25 – 29 June 2018, Berlin, Germany*, no. 3, pp. 941–950, 2018.

[23] R. De Finis, D. Palumbo, M. Da Silva, and U. Galietti, "Is the temperature plateau of a self-heating test a robust parameter to investigate the fatigue limit of steels with thermography?," *Fatigue & Fracture of Engineering Materials & Structures*, vol. 41, no. 4, pp. 917–934, 2018.

[24] G. Meneghetti and M. Ricotta, "Estimating the intrinsic dissipation using the second harmonic of the temperature signal in tension-compression fatigue: Part I. theory," *Fatigue & Fracture of Engineering Materials & Structures*, 2021.

[25] D. Shiozawa, T. Inagawa, T. Washio, and T. Sakagami, "Fatigue limit estimation of stainless steels with new dissipated energy data analysis," *Procedia Structural Integrity*, vol. 2, pp. 2091–2096, 2016.

[26] R. De Finis, D. Palumbo, and U. Galietti, "On the relationship between mechanical energy rate and heat dissipated rate during fatigue for a c45 steel depending on stress ratio," *Fatigue & Fracture of Engineering Materials & Structures*, vol. 44, no. 10, pp. 2781–2799, 2021.

[27] S. Quinn, J. Dulieu-Barton, and J. Langlands, "Progress in thermoelastic residual stress measurement," *Strain*, vol. 40, no. 3, pp. 127–133, 2004.

[28] R. De Finis, D. Palumbo, A. Pirinu, A. Saponaro, F. Panella, R. Nobile, and U. Galietti, "Fatigue behaviour assessment of C45 steel by means of energy-based methods," in *IOP Conference Series: Materials Science and Engineering*, vol. 1038, p. 012015, IOP Publishing, 2021.

[29] N. Rajic and N. Street, "A performance comparison between cooled and uncooled infrared detectors for thermoelastic stress analysis," *Quantitative InfraRed Thermography Journal*, vol. 11, no. 2, pp. 207–221, 2014.

[30] G. Pitarresi, R. Cappello, and G. Catalanotti, "Quantitative thermoelastic stress analysis by means of low-cost setups," *Optics and Lasers in Engineering*, vol. 134, p. 106158, 2020.

[31] R. De Finis, D. Palumbo, and U. Galietti, "Mechanical Behaviour of Stainless Steels under Dynamic Loading: An Investigation with Thermal Methods," *Journal of Imaging*, vol. 2, no. 4, 2016.

[32] R. Urbanek and J. Baer, "Influence of motion compensation on lock-in thermographic investigations of fatigue crack propagation," *Engineering Fracture Mechanics*, vol. 183, pp. 13–25, 2017.

[33] R. Barbagallo, G. Fargione, F. Giudice, and G. La Rosa, "Thermographic-dic approach in fatigue behaviour analysis," in *IOP Conference Series: Materials Science and Engineering*, vol. 1038, p. 012050, IOP Publishing, 2021.

[34] R. Peyroux, A. Chrysochoos, C. Licht, and M. Löbel, "Thermomechanical couplings and pseudoelasticity of shape memory alloys," *International Journal of Engineering Science*, vol. 36, no. 4, pp. 489–509, 1998.

[35] A. Chrysochoos and H. Louche, "An infrared image processing to analyse the calorific effects accompanying strain localisation," *International journal of engineering science*, vol. 38, no. 16, pp. 1759–1788, 2000.

[36] N. F. Enke, "An enhanced theory for thermographic stress analysis of isotropic materials," in *Stress and Vibration: Recent Developments in Industrial Measurement and Analysis*, vol. 1084, pp. 84–102, International Society for Optics and Photonics, 1989.

[37] P. Bremond and P. Potet, "Lock-in thermography: a tool to analyze and locate thermomechanical mechanisms in materials and structures," in *Thermosense XXIII*, vol. 4360, pp. 560–566, International Society for Optics and Photonics, 2001.

[38] J. Lemaitre and J.-L. Chaboche, *Mechanics of solid materials*. Cambridge university press, 1994.

[39] A. Chrysochoos, B. Berthel, F. Latourte, A. Galtier, S. Pagano, and B. Wattrisse, "Local energy analysis of high-cycle fatigue using digital image correlation and infrared thermography," *The Journal of Strain Analysis for Engineering Design*, vol. 43, no. 6, pp. 411–422, 2008.

[40] G. Pitarresi and E. Patterson, "A review of the general theory of thermoelastic stress analysis," *The Journal of Strain Analysis for Engineering Design*, vol. 38, no. 5, pp. 405–417, 2003.

[41] A. Wong, R. Jones, and J. Sparrow, "Thermoelastic constant or thermoelastic parameter?," *Journal of Physics and chemistry of solids*, vol. 48, no. 8, pp. 749–753, 1987.

[42] A. Wong, J. Sparrow, and S. Dunn, "On the revised theory of the thermoelastic effect," *Journal of Physics and chemistry of solids*, vol. 49, no. 4, pp. 395–400, 1988.

[43] S. Dunn, "Using nonlinearities for improved stress analysis by thermoelastic techniques," 1997.

[44] J. Eaton-Evans, J. Dulieu-Barton, E. Little, and I. Brown, "Thermoelastic studies on nitinol stents," *The Journal of Strain Analysis for Engineering Design*, vol. 41, no. 7, pp. 481–495, 2006.

[45] P. Seelan, J. Dulieu-Barton, and F. Pierron, "Microstructural assessment of 316l stainless steel using infrared thermography based measurement of energy dissipation arising from cyclic loading," *Mechanics of Materials*, vol. 148, p. 103455, 2020.

[46] C. Bubulinca, X. Balandraud, M. Grédiac, S. Stanciu, and M. Abrudeanu, "Characterization of the mechanical dissipation in shape-memory alloys during stress-induced phase transformation," *Journal of Materials Science*, vol. 49, no. 2, pp. 701–709, 2014.

[47] B. Atzori and G. Meneghetti, "Energy Dissipation in Low Cycle Fatigue of Austempered Ductile Irons," in *5th International Conference on Low Cycle Fatigue*, 2003.

[48] J. Bär, L. Seilnacht, and R. Urbanek, "Determination of dissipated energies during fatigue tests on copper and aa7475 with infrared thermography," *Procedia Structural Integrity*, vol. 17, pp. 308–315, 2019.

[49] J. Bär and R. Urbanek, "Determination of dissipated energy in fatigue crack propagation experiments with lock-in thermography," *Frattura ed Integrità Strutturale*, vol. 13, no. 48, pp. 563–570, 2019.

[50] D. Palumbo, R. De Finis, F. Ancona, and U. Galietti, "Damage monitoring in fracture mechanics by evaluation of the heat dissipated in the cyclic plastic zone ahead of the crack tip with thermal measurements," *Engineering Fracture Mechanics*, vol. 181, pp. 65–76, 2017.

Appendix A

A simple simulation of the thermoelastic effect induced temperature change, $E = \Delta T$, is reported here with the purpose to estimate the sensitivity of this metric to an increase of the mean temperature of the material.

It is useful to recall the first order thermoelastic law in the form:

$$E = |\Delta T| = T_o K_o \Delta \sigma_{xx} \tag{A-1}$$

The C45 thermoelastic constant is assumed to be 3.2×10^{-6} 1/MPa, which is a value in good agreement with data in the literature and with the experiments performed in this work [2]. For simplicity, it is also assumed that this value of K_o stays constant throughout all the range of stress amplitudes considered.

The material average temperature follows two different scenarios, reported in Table 5.

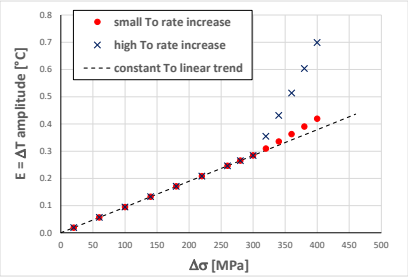

Figure 28: E vs σ_a plots from data in Table 5.

The first scenario (second column in Table 5) considers a slight increase of T_o for $\sigma_a > 300$ MPa (in agreement with tests at $R = -1$), with a rate comparable to the experimental values measured in this work (see Fig. 28), and with a constant room temperature of $T_o = 296$ K for $\sigma_a < 300 MPa$. The second scenario (forth column in Table 5) considers a higher rate of temperature increase for $\sigma_a > 300$ MPa, in agreement with experimental data reported in [2, 28].

Table 5: Thermoelastic signal expected from C45 steel with simulated rates of increase of T_o for increasing stress amplitude.

Thermoelastic constant for C45: 3.2×10^{-6} [1/MPa]				
	small T_o rate increase		high T_o rate increase	
σ_a	T_o	E	T_o	E
20	296	0.02	296	0.02
60	296	0.06	296	0.06
100	296	0.09	296	0.09
140	296	0.13	296	0.13
180	296	0.17	296	0.17
220	296	0.21	296	0.21
260	296	0.25	296	0.25
280	296	0.27	296	0.27
300	296	0.28	296	0.28
320	302.25	0.31	346	0.35
340	308.5	0.34	396	0.43
360	314.75	0.36	446	0.51
380	321	0.39	496	0.60
400	327.25	0.42	546	0.70

Figure 28 shows the trend of E vs σ_a as predicted by eq. A-1 and the two scenarios in Table 5. It is seen that if the material in the FLTM scheme exhibits a significant rate of temperature increase, this has a non-negligible impact on the thermoelastic signal and its deviation from linearity.

If the increase of T_o is to be correlated with the onset of dissipation and damage, than, indirectly, a signature of this is also obtained with the E metric through its dependence from T_o. The present work, though, finds that the rate of increase of T_o is also highly sensitive to the loading frequency.